Direct optimization of continuous non-intersecting toolpaths for extrusion-based 3D printing

Emad Shakur[1*] and Oded Amir[1]

[1*]Technion – Israel Institute of Technology, Technion City, Haifa, 3200003, Israel.

*Corresponding author(s). E-mail(s): semad@technion.ac.il;

Abstract

We present a novel framework for the direct optimization of continuous, non-intersecting toolpaths in extrusion-based additive manufacturing. The toolpath parameterization serves both as an explicit representation of the geometry and as the optimization design variables, eliminating the need for intermediate design representations and post-processing for generating a manufacturable toolpath, thereby closing the gap between design and fabrication. The toolpath is represented by a continuous piecewise-linear centerline that is controlled by shape design variables. Finite element analysis for evaluating structural and thermal responses is achieved by a distance-based embedding technique within a fixed grid. Physical manufacturability is enforced throughout the optimization using differentiable geometric constraints that ensure minimum filament spacing, prevent self-intersections, control local toolpath angles, and preserve prescribed material-free regions. Inspired by potential applications in 3D printing of cementitious materials, the efficacy of the framework is demonstrated primarily by applications in cross-section layout design of masonry blocks and walls, considering structural and thermal performances. The numerical examples show that the proposed approach generates toolpath-based layouts that are straightforward to manufacture, while providing systematic control over structural stiffness and thermal insulation.

Keywords: Structural optimization, Toolpath optimization, Extrusion-based additive manufacturing, 3D concrete printing, Manufacturability constraints

1 Introduction

Additive manufacturing enables the fabrication of geometrically complex structures through layer-wise material deposition, offering substantially greater geometric freedom than conventional manufacturing techniques. Consequently, considerable research has been devoted to printable materials, fabrication processes, and the integration of additive manufacturing into engineering design. This expanded geometric freedom has created new opportunities for design methodologies that seek highly efficient material layouts, particularly structural optimization. By enabling the fabrication of geometries that would be impractical to manufacture using conventional techniques, additive manufacturing has made the realization of optimized structural designs increasingly feasible. Nevertheless, several challenges must be addressed to fully exploit the benefits of integrating additive manufacturing with structural optimization.

A major challenge is the transition between optimized material layouts and the actual toolpaths used during fabrication. Several studies investigated the generation of structurally informed toolpaths for additive manufacturing. Stress- and field-aligned path-planning strategies have been proposed to improve the structural performance of printed components by aligning deposition trajectories with principal stresses or prescribed orientation fields (Sales et al. 2021; Chen et al. 2022; Kubalak et al. 2024; Fang et al. 2024). Although these approaches strengthen the relationship between structural response and fabrication, they primarily address toolpath planning for prescribed geometries rather than the structural optimization of the deposition path itself.

Other studies sought to integrate structural optimization more closely with toolpath planning by incorporating manufacturing considerations directly into the optimization process. Concurrent design frameworks have been proposed in which structural optimization is coupled with toolpath generation or printing strategy optimization (Ren et al. 2024; Kubalak et al. 2025). In parallel, deposition-related manufacturing constraints, including nozzle size, bead width, bonding behavior, and printing-induced anisotropy, have been incorporated directly into topology optimization formulations (Carstensen 2020; Kim-Tackowiak and Carstensen 2025). While these methods improve manufacturability and strengthen the coupling between design and fabrication, the underlying design representation remains a topology or material distribution, with printable toolpaths derived as a secondary representation.

Related developments have explored also the explicit representation and optimization of manufacturing paths. Boissier et al. (2020) employed shape optimization techniques to optimize laser scanning trajectories for powder-bed fusion while accounting for thermal considerations. In the context of continuous fiber-reinforced additive manufacturing, Greifenstein et al. (2023) introduced an explicit feature-mapping framework in which fiber features are represented by parameterized splines and optimized while satisfying manufacturing constraints such as a minimum turning radius. Building on this spline-based representation, Wein et al. (2025) developed a methodology for generating manufacturable spline toolpaths for continuous fiber deposition within prescribed structural designs while enforcing geometric constraints such as minimum turning radius, parallel path spacing, and non-intersecting trajectories. More recently, Guo et al. (2026) proposed a B-spline-driven topology and fiber-path optimization framework in which the structural geometry is represented by a set of variable-width B-spline components, while continuous fiber paths are generated as iso-contours of a distance-induced scalar field. Collectively, these studies demonstrate the potential of explicit geometric representations for manufacturing path optimization. However, in these approaches, the printable toolpath itself is not treated as the primary geometric design representation and optimization variable.

Among extrusion-based additive manufacturing technologies, 3D concrete printing (3DCP) has attracted particular attention in civil engineering owing to its potential to transform conventional construction practices while reducing the environmental impact of the cement and concrete industries. Applications include printed walls, masonry units, façade elements, formwork-free concrete components, and optimized structures. Recent reviews highlight the rapid growth of the field, with applications ranging from small-scale prototypes to full-scale buildings and infrastructure projects (Hasani and Dorafshan 2024). Compared with polymer- or metal-based additive manufacturing processes, 3DCP introduces additional challenges related to material rheology, layer bonding, buildability, and the continuity of the deposited path. Furthermore, because the deposited filaments are typically several centimeters wide, the toolpath has a much greater influence on the geometry, material distribution, and connectivity of the final structure, making careful toolpath design a central consideration in manufacturing-aware structural optimization.

As 3D concrete printing has evolved from architectural and non-structural applications toward load-bearing structures, increasing attention has been devoted to improving structural performance through compression-oriented structural forms, prestressing and post-tensioning techniques, and strategies to mitigate weak interlayer bonding, thereby expanding the range of feasible structural applications (Bhooshan et al. 2022; Li et al. 2024; Salet et al. 2018; Gebhard et al. 2021; Coward and Sørensen 2023; Wang et al. 2020; Moelich et al. 2021; Maroszek et al. 2025; Sun et al. 2026). Despite these advances, the fabrication of geometrically complex optimized structures remains challenging, motivating design methodologies that more closely reflect the capabilities and constraints of the fabrication process. In this context, Breseghello and Naboni (2022) proposed a fabrication-aware design workflow that integrates stress-based design, geometric toolpath optimization, and reinforcement planning for 3D concrete printing, demonstrating the benefits of integrating structural design and fabrication within a unified workflow. Hybrid construction, in which 3D printing is used to fabricate stay-in-place formwork that is subsequently filled with conventionally cast concrete, combines the geometric freedom of additive manufacturing with the structural performance of cast concrete and has been successfully applied to a variety of structural applications (Anton et al. 2021; Zhu et al. 2021; Chen et al. 2023; Maitenaz et al. 2024; Bai et al. 2024; Raza et al. 2025; Sakha et al. 2026; Shakur and Amir 2026).

Despite these advances, optimization frameworks that directly treat the printable toolpath as both the primary geometric representation and the optimization variable remain rare, particularly in the context of 3D concrete printing. One recent development in this direction was presented by Kim-Tackowiak et al. (2026), who parameterized the printable toolpath through a truss ground structure containing the possible member configurations, and employed a mixed-integer nonlinear programming topology optimization framework to identify a structurally optimized path satisfying fabrication requirements. Nevertheless, the vast majority of existing approaches rely on intermediate design representations, such as density fields, boundaries, or lattice layouts, from which printable toolpaths are subsequently generated. Consequently, discrepancies may arise between the optimized and fabricated geometries, while the printable toolpath itself is generally not treated as the primary geometric design representation and optimization variable.

These limitations motivate the toolpath-based optimization framework proposed in this work, which provides an alternative direction to the truss-based formulation of Kim-Tackowiak et al. (2026) by directly parameterizing and optimizing the shape of the printable toolpath. The printable toolpath serves as both the primary geometric representation and as the set of design variables. The framework directly optimizes continuous, non-intersecting printable toolpaths while incorporating fabrication constraints throughout the optimization process. The proposed formulation establishes a unified representation of design and manufacturing by eliminating the need for intermediate geometric reconstruction, thereby enabling the direct optimization of fabrication-ready deposition paths. While our work is driven by applications in printing of cementitious materials, the approach is nevertheless general and can be applied in various scenarios that require continuous, non-intersecting toolpaths.

The proposed framework is demonstrated on cross-sectional design of wall systems and masonry blocks, as well as on beam geometries. The former two cases involve the optimization with respect to mechanical and thermal performances, a problem of particular interest in masonry units and building envelopes because structural load-carrying capacity and thermal insulation are often competing design objectives. Previous studies have investigated topology and geometry optimization for improving these performance measures (Sousa et al. 2011; Bruggi and Taliercio 2013; Vantyghem et al. 2016). Herein, the mechanical and thermal optimization problems are adopted as representative applications to demonstrate the capabilities and generality of the proposed framework.

The remainder of this paper is organized as follows. In Section 2 we present the toolpath-based optimization framework, including the geometric representation. In Section 3 we describe the analysis models for the mechanical and thermal problems. Section 4 is dedicated to the optimization formulations and the corresponding sensitivity analyses, and several demonstrative case studies are presented in Section 5. Finally, in Section 6 we summarize the main findings and outline directions for future research.

2 Design parametrization

In this work, geometry is represented explicitly through the toolpath centerline, which defines the printed structure. At this point, the formulation is developed in two dimensions for cross-sectional designs that remain uniform along the third dimension, whereas three-dimensional variations will be considered in future work. The toolpath is modeled as a continuous piecewise linear curve, whose shape within the domain is controlled by the design variables.

The considered configurations consist of a prescribed number of perimeter toolpaths together with an internal infill pattern, whose shape is determined by the design variables. Assuming a rectangular outer boundary, the perimeter layers are placed along the boundary, while the interior region is generated by multiple zigzag paths. Figures 1–3 illustrate the adopted parametrization and corresponding geometric definitions, with Figure 1 showing an illustrative example of the toolpath arrangement within the rectangular domain, interpreted as follows:

1. The black rectangle denotes the outer boundary of the design domain, defined by dimensions l_x and l_y.
2. The perimeter consists of N_{outer} perimeter toolpath layers; in the illustrated example, two layers are used.
3. The interior region is filled with zigzag paths forming rhombic cells. The number of cells in the x- and y-directions is denoted by N_{rx} and N_{ry}, respectively; in the illustrated example, $N_{\mathrm{rx}} = 4$ and $N_{\mathrm{ry}} = 3$.
4. Each edge of a rhombus is discretized into N_{seg} linear segments; in the illustrated example, $N_{\mathrm{seg}} = 4$.

5. The vertices of the rhombic cells are locally truncated and shifted to create finite shared interfaces, thereby improving structural continuity and interlayer bonding, as illustrated by the region highlighted by the black circle in Figure 1.
6. The toolpath width is denoted by t_w. Neighboring toolpaths are arranged according to a prescribed spacing ratio α, where the center-to-center distance between adjacent filaments equals αt_w. This results in an overlap ratio of $1-\alpha$; for instance, $\alpha = 0.9$ corresponds to a 10% overlap between adjacent filaments. Figure 2 illustrates this overlap configuration, where the gray region denotes the deposited material.
7. To ensure a continuous and non-intersecting toolpath, the perimeter layers are constructed according to the scheme illustrated in Figure 3, where the corresponding start and end regions are designed to maintain a prescribed spacing of αt_w between adjacent segments.

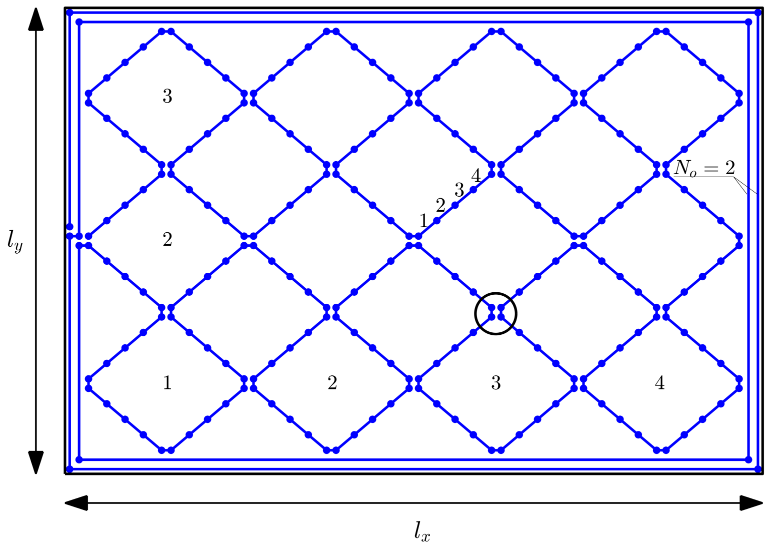

Fig. 1: Illustration of the proposed continuous, non-intersecting toolpath parametrization for a rectangular domain. The outer boundary is defined by dimensions l_x and l_y, with $N_{\text{outer}} = 2$ perimeter layers and a zigzag infill pattern forming rhombic cells. The number of cells in this example in the x- and y-directions is $N_{\text{rx}} = 4$ and $N_{\text{ry}} = 3$, respectively. Each edge is discretized into $N_{\text{seg}} = 4$ linear segments.

To control the toolpath geometry, the control points are classified into three categories, designated in red, green, and blue, as shown in Figure 4.

1. Red points represent independent design variables, whose x- and y-coordinates are directly optimized.
2. Green control points are located within the connection regions between adjacent rhombic cells and between rhombic cells and the perimeter toolpath segments. Their motion is governed by artificial reference points positioned at their mean locations while maintaining prescribed relative distances, as illustrated in Figure 5. These artificial reference points are denoted in magenta in the figures. Figure 5a shows the reference points at interfaces between neighboring cells, where movement is permitted in both the x- and y-directions. Figure 5b illustrates the corresponding reference points between vertex regions and perimeter layers, where movement is restricted to the direction parallel to the associated perimeter. The allowable movement directions are indicated by black arrows.
3. Blue control points remain fixed throughout the optimization process.

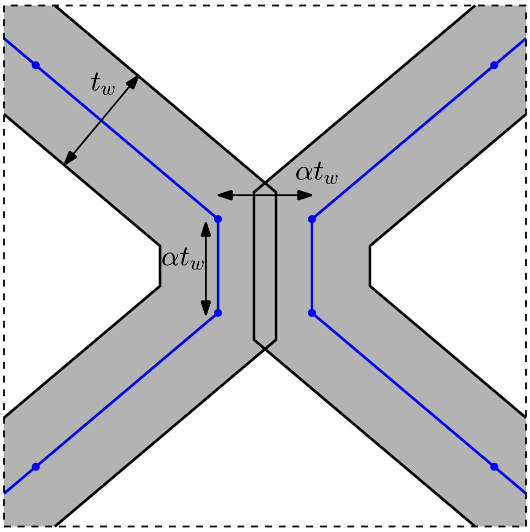

Fig. 2: Zoom-in view of the connection between two adjacent rhombic cells. The gray-filled region represents the physical width of the toolpath, illustrating the overlap-controlled spacing.

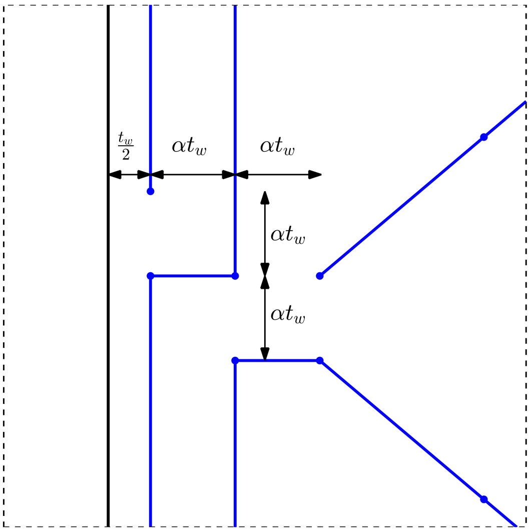

Fig. 3: Zoom-in view of the toolpath start/end region,illustrating the spacing between adjacent segments.

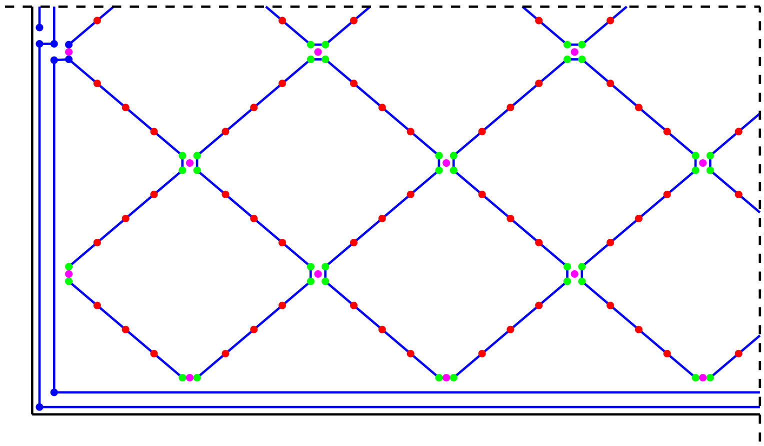

Fig. 4: Classification of toolpath control points used for geometric parametrization and optimization. Red points denote independent design variables, green points denote dependent control points, magenta points denote the artificial reference points governing the motion of the green points, and blue points denote fixed control points.

3 Finite element analysis

In this work, the structural and thermal responses are analyzed using finite elements in a domain denoted by Ω, with boundary $\partial\Omega$. The corresponding governing equations and finite element formulations are presented in the following sections.

3.1 Pseudo-density distribution

The design domain is represented using a structured finite element mesh composed of four-node quadrilateral elements, together with a density-based embedding approach to distinguish between material and void regions. Each element is assigned a continuous pseudo-density parameter $\rho_i \in [0, 1]$, from which the corresponding material properties are evaluated.

Element pseudo-densities are determined through two sequential stages. In the first stage, a super-Gaussian distance-based filter is applied based on the distance d_i between the element centroid and the toolpath centerline, resulting in an intermediate density field denoted by ρ_i. The distance field depends on the shape design variables $\mathbf{X}$ that control the geometry of the toolpath. The distance

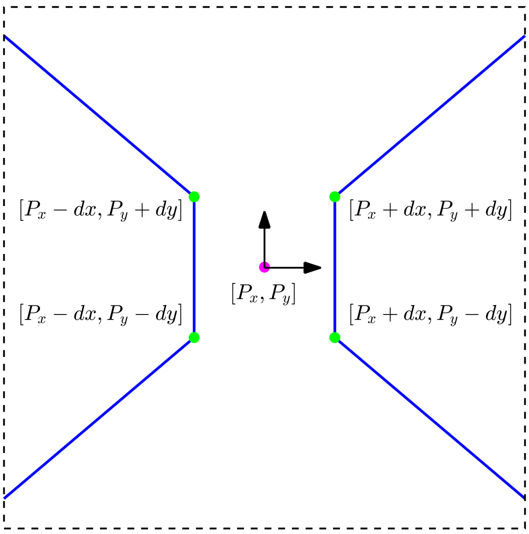

(a) Reference-point parametrization at interfaces between adjacent cells, with allowable motion in both the x- and y-directions.

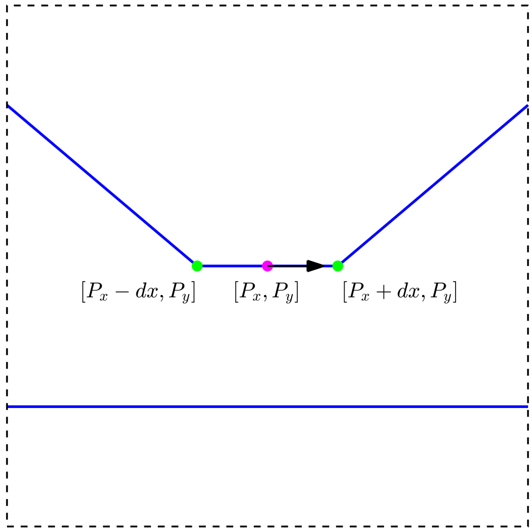

(b) Reference-point parametrization between vertex regions and perimeter layers, with motion constrained parallel to the corresponding perimeter.

Fig. 5: Parametrization of dependent green control points using artificial reference points (magenta) in different connection regions. Black arrows indicate the allowable directions of motion of the associated reference points.

d_i is computed as the minimum distance between the element centroid and all individual toolpath segments. While the distance to each individual toolpath segment is smooth, the sensitivity of the minimum-distance function may be discontinuous when the active closest segment changes. Nevertheless, stable convergence was observed throughout all case studies presented in Section 5. If numerical instabilities arise from such changes, smooth minimum-distance approximations, such as p-norm aggregation, may be employed to obtain smoother sensitivities. In the second stage, this density field is regularized using a smoothed Heaviside projection to sharpen the material–void transition, producing the final density field $\bar{\rho}_i$, which is used in the analysis:

$$\bar{\rho}_i = \mathcal{H}\big(\rho_i(d_i(\mathbf{X}))\big), \tag{1}$$

where $\mathcal{H}(\cdot)$ denotes the smoothed Heaviside projection operator.

The initial element density is defined such that solid material is assigned to elements located within a distance of $t_w/2$ (half the toolpath width) from the toolpath centerline, while smoothly decaying toward void elsewhere:

$$\rho_i = e^{-\left(\frac{d_i}{\beta}\right)^{p_f}}, \tag{2}$$

where p_f controls the sharpness of the density transition, and β is selected such that $\rho_i = 0.5$ at $d_i = t_w/2$, yielding

$$\beta = \frac{t_w/2}{(-\ln(0.5))^{1/p_f}}. \tag{3}$$

The filtered density field is subsequently projected using the smoothed Heaviside function

$$\bar{\rho}_i = \frac{\tanh(\beta_{\mathrm{HV}}\eta) + \tanh(\beta_{\mathrm{HV}}\,(\rho_i - \eta))}{\tanh(\beta_{\mathrm{HV}}\eta) + \tanh(\beta_{\mathrm{HV}}(1-\eta))}, \tag{4}$$

where β_{HV} controls the sharpness of the Heaviside projection, and η defines the threshold value separating material and void regions, herein chosen as $\eta = 0.5$.

Figure 6 illustrates the relationship between the distance from the toolpath centerline and the resulting element density for representative values of $p_f = 6$ and $\beta_{\mathrm{HV}} = 16$. This two-step formulation effectively captures the physical width of the deposited toolpath while maintaining a stable and well-defined material–void transition. In contrast, achieving a similarly sharp transition without the Heaviside projection would require significantly larger values of p_f, which may compromise the numerical robustness.

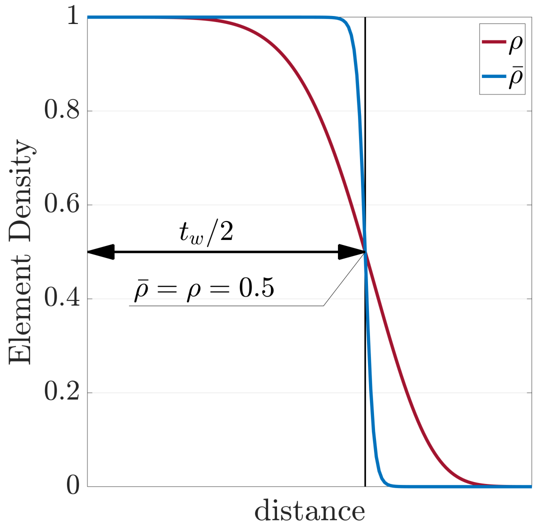

Fig. 6: Element density as a function of the distance from the toolpath centerline for $p_f = 6$ and $\beta_{\mathrm{HV}} = 16$. The super-Gaussian filter generates the initial density field, while the Heaviside projection sharpens the material–void transition.

Based on this formulation, the finite element density field associated with the toolpath geometry shown in Figure 1 is presented in Figure 7a, together with enlarged views of the regions indicated by the dashed black squares in Figures 7b and 7c. In the enlarged views, the toolpath side boundaries corresponding to the deposited toolpath width are shown in green. For the density field shown in these figures, the ratio of the finite element size to the toolpath width is approximately 1 : 10.

3.2 Governing equations for structural applications

The structural response is modeled under assumptions of a linear elastic continuum, using the pseudo-density field within the finite element mesh defined in the previous subsection. The displacement field $\mathbf{u}(\mathbf{x})$ satisfies

$$\nabla \cdot \boldsymbol{\sigma} = \mathbf{0} \quad \text{in } \Omega, \qquad \boldsymbol{\sigma} = \mathbb{C} : \boldsymbol{\varepsilon}(\mathbf{u}), \tag{5}$$

where $\mathbb{C}$ is the elasticity tensor and $\boldsymbol{\varepsilon}(\mathbf{u})$ is the infinitesimal strain tensor. Employing a standard finite element framework, the corresponding discrete system is given by

$$\mathbf{K}_m \mathbf{u} = \mathbf{F}_m, \tag{6}$$

where $\mathbf{K}_m$ is the global mechanical stiffness matrix assembled from the elemental stiffness matrices, and $\mathbf{F}_m$ is the global external load vector assembled from the elemental load contributions. Dirichlet boundary conditions are imposed on the displacement field according to the prescribed support conditions of each case study. The elastic modulus of each element is interpolated using the RAMP function (Stolpe and Svanberg 2001) according to its pseudo-density as

$$E_i(\bar{\rho}_i) = E_{\min} + \frac{\bar{\rho}_i}{1 + q_m(1 - \bar{\rho}_i)} \left(E_{\max} - E_{\min} \right), \tag{7}$$

where $E_{\max}$ denotes the elastic modulus of the solid material; $E_{\min}$ is a small regularization parameter introduced to prevent singularities in the stiffness matrix; and q_m is the mechanical penalization parameter controlling the interpolation between void and solid phases. To quantify the structural performance, the mechanical compliance is adopted as the objective measure, written in discrete form as

$$C = \mathbf{u}^T \mathbf{K}_m \mathbf{u} = \mathbf{F}_m^T \mathbf{u}, \tag{8}$$

which is minimized to maximize the structural stiffness.

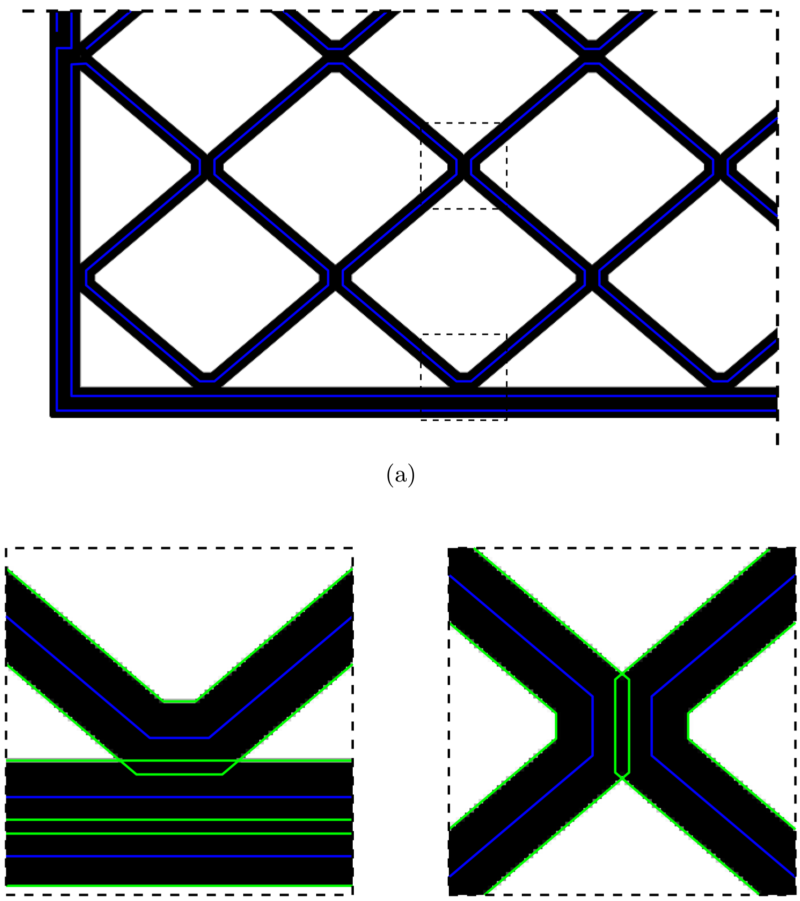

(a)

(b) (c)

Fig. 7: Finite element density field corresponding to the toolpath geometry shown in Figure 1. Enlarged views of selected regions, indicated by dashed black squares, illustrate the density distribution near representative toolpath features and connection zones. The toolpath side boundaries corresponding to the deposited toolpath width are shown in green in the enlarged views.

3.3 Governing equations for thermal applications

The thermal behavior is modeled as a steady-state heat conduction problem using the pseudo-density field within the finite element mesh defined in the previous subsection. Assuming isotropic material behavior and neglecting internal volumetric heat generation, the temperature field $T(\mathbf{x})$ satisfies

$$k\Delta T = 0 \qquad \text{in } \Omega, \tag{9}$$

where k denotes the thermal conductivity of the material. The boundary $\partial\Omega$ is partitioned as

$$\partial\Omega = \Gamma_T \cup \Gamma_q \cup \Gamma_c,$$

where Γ_T, Γ_q, and Γ_c denote Dirichlet, Neumann, and Robin (convective) boundaries, respectively. The corresponding boundary conditions are

$$T = T_0 \qquad \text{on } \Gamma_T, \tag{10}$$

$$-k\nabla T \cdot \mathbf{n} = q \qquad \text{on } \Gamma_q, \tag{11}$$

$$-k\nabla T \cdot \mathbf{n} = h_c(T - T_a) \qquad \text{on } \Gamma_c, \tag{12}$$

where $\mathbf{n}$ is the outward unit normal vector; T_0 is the prescribed temperature on Dirichlet boundaries; q is the prescribed heat flux on Neumann boundaries; h_c is the convective heat transfer coefficient; and T_a denotes the ambient temperature associated with the surrounding environment. Within the finite element framework, discretization of these governing equations yields the linear system

$$\mathbf{K}_t\mathbf{T} = \mathbf{F}_t, \tag{13}$$

where $\mathbf{T}$ is the vector of nodal temperatures and

$$\mathbf{K}_t = \mathbf{K}_{\text{cond}} + \mathbf{H} \tag{14}$$

is the global thermal stiffness matrix. The corresponding thermal load vector is given by

$$\mathbf{F}_t = \mathbf{H}\mathbf{T}_a, \tag{15}$$

where $\mathbf{K}_{\text{cond}}$ represents the contribution of conduction assembled over the domain, while $\mathbf{H}$ corresponds to the conduction of convection assembled over the convective boundaries.

Similarly to Young's modulus, the thermal conductivity of each element is interpolated according to its pseudo-density using RAMP,

$$k_i(\bar{\rho}_i) = k_{\min} + \frac{\bar{\rho}_i}{1 + q_t(1-\bar{\rho}_i)}\left(k_{\max} - k_{\min}\right), \tag{16}$$

where $k_{\max}$ and $k_{\min}$ denote the thermal conductivities of the solid and void phases, respectively; and q_t is the thermal penalization parameter controlling the interpolation between both phases.

For the building-envelope configurations considered in this work, the convective boundary is divided into internal and external surfaces, with prescribed indoor and outdoor ambient temperatures denoted by T_{in} and T_{out}, and corresponding convective heat transfer coefficients denoted by h_{in} and h_{out}, respectively. Thermal insulation performance is quantified directly using the thermal transmittance (U-value), which is widely adopted in building physics to measure the average heat transfer through an envelope. The U-value is defined as

$$U = \frac{1}{|\Gamma_{\text{in}}|}\int_{\Gamma_{\text{in}}} h_{\text{in}}\left(T_{\text{in}} - T\right)\, d\Gamma, \tag{17}$$

where Γ_{in} denotes the internal convective boundary and h_{in} is the indoor convective heat transfer coefficient. The quantity

$$h_{\text{in}}\left(T_{\text{in}} - T\right)$$

represents the local convective heat flux transferred from the indoor environment to the structure, while integration over the internal surface and normalization by its length yield the average thermal transmittance. Lower values of U correspond to reduced heat transfer through the structure and therefore improved thermal insulation performance. Accordingly, the U-value in this work is either minimized directly or imposed as a design constraint, depending on the considered optimization formulation, to achieve the desired thermal resistance of the optimized geometry.

4 Optimization formulations

In this work, the proposed framework is applied to three types of optimization settings: (i) Minimization of mechanical compliance; (ii) Minimization of thermal transmittance, quantified by the U-value in (17); and (iii) Minimization of mechanical compliance subject to an upper bound on the thermal transmittance to ensure a prescribed insulation performance. In all formulations, geometric regularization constraints are imposed to prevent intersecting toolpath segments and enforce the required clearance between neighboring toolpaths, thereby ensuring manufacturable designs.

The three optimization formulations are defined as follows. For mechanical compliance minimization,

$$\begin{aligned}
\min_{\mathbf{X}} \quad & C = \sum_{i=1}^{N_L} w_i\, \mathbf{F}_{m,i}^T \mathbf{u}_i \\
\text{s.t.} \quad & \mathbf{g}_{\text{geo}}(\mathbf{X}) \leq \mathbf{0} \\
& \underline{\mathbf{X}} \leq \mathbf{X} \leq \overline{\mathbf{X}} \\
& \mathbf{K}_m(\mathbf{X})\mathbf{u}_i = \mathbf{F}_{m,i}, \qquad i = 1, \ldots, N_L,
\end{aligned} \tag{18}$$

for thermal transmittance minimization,

$$\begin{aligned} \min_{\mathbf{X}} \quad & U(\mathbf{X}) \\ \text{s.t.} \quad & \mathbf{g}_{\text{geo}}(\mathbf{X}) \leq \mathbf{0} \\ & \underline{\mathbf{X}} \leq \mathbf{X} \leq \overline{\mathbf{X}} \\ & \mathbf{K}_t(\mathbf{X})\mathbf{T} = \mathbf{F}_t, \end{aligned} \tag{19}$$

and for mechanical compliance minimization with a constraint on thermal performance,

$$\begin{aligned} \min_{\mathbf{X}} \quad & C = \sum_{i=1}^{N_L} w_i\, \mathbf{F}_{m,i}^T \mathbf{u}_i \\ \text{s.t.} \quad & U(\mathbf{X}) \leq U_{\max} \\ & \mathbf{g}_{\text{geo}}(\mathbf{X}) \leq \mathbf{0} \\ & \underline{\mathbf{X}} \leq \mathbf{X} \leq \overline{\mathbf{X}} \\ & \mathbf{K}_m(\mathbf{X})\mathbf{u}_i = \mathbf{F}_{m,i}, \qquad i = 1, \ldots, N_L \\ & \mathbf{K}_t(\mathbf{X})\mathbf{T} = \mathbf{F}_t. \end{aligned} \tag{20}$$

In the formulation above, $\underline{\mathbf{X}}$ and $\overline{\mathbf{X}}$ denote the lower and upper bounds on the design variables, respectively; $\mathbf{g}_{\text{geo}}(\mathbf{X})$ denotes the vector of geometric regularization constraints, elaborated in the following subsection; N_L denotes the number of mechanical load cases; and w_i is the weighting factor associated with load case i.

4.1 Geometric regularization constraints

The geometric regularization constraints $\mathbf{g}_{\text{geo}}(\mathbf{X})$ consist of three constraint groups: (i) A clearance and non-intersection constraint to prevent local geometric violations and ensure manufacturable toolpaths; (ii) A fixed-void constraint that preserves prescribed material-free regions; and (iii) An angular regularization constraint comprising lower and upper bounds on the angles between neighboring toolpath segments, to avoid excessively sharp or overly flat geometric transitions.

4.1.1 Clearance and non-intersecting constraint

Shape optimization, combined with the free movement of control points according to the toolpath parameterization described in Section 2, may produce geometric violations such as direct intersections between neighboring toolpath segments (Figure 8a) or insufficient spacing below the prescribed clearance associated with the toolpath width (Figure 8b). Such configurations violate manufacturability requirements and may lead to physically infeasible printing paths. To ensure fabrication feasibility, a geometric clearance constraint is introduced to prevent both intersecting segments and insufficient local spacing.

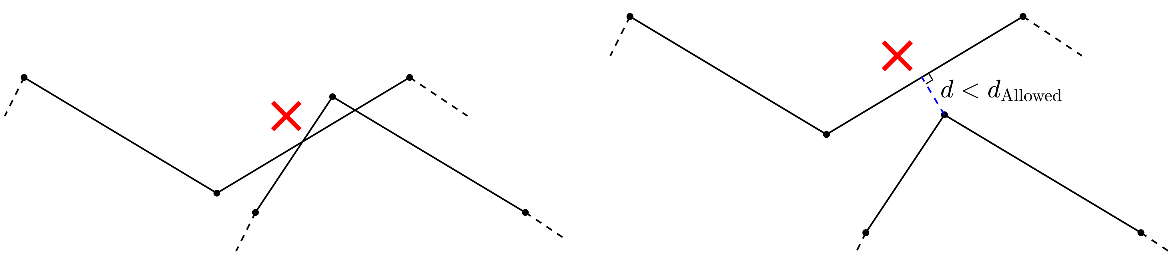

(a) (b)

Fig. 8: Examples of geometric infeasibility during toolpath optimization. (a) Self-intersecting toolpath and (b) violation of the minimum allowable clearance between adjacent toolpath segments.

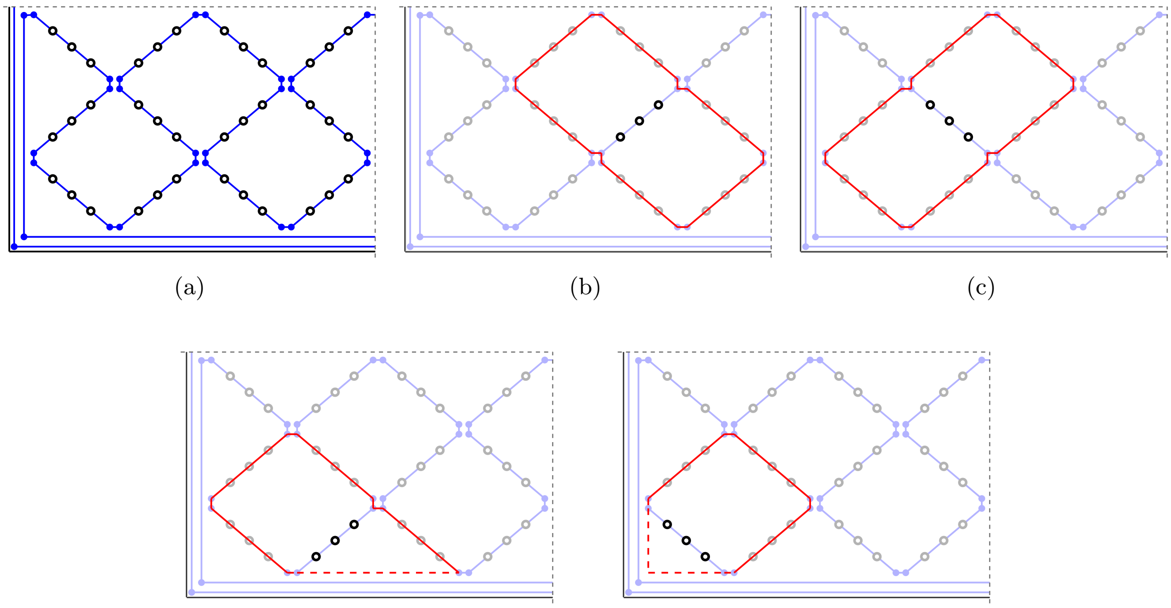

(a) (b) (c)

(d) (e)

Fig. 9: Construction of the polygonal admissible regions Γ_i associated with representative local toolpath cells. Hollow black markers denote the selected critical control points $\{\mathbf{p}_i\}_{i=1}^{N_p}$, while solid and dashed red lines indicate the boundaries of the corresponding admissible polygons. Dashed red segments represent portions of Γ_i that do not coincide with the physical toolpath geometry.

To enforce this constraint, a set of critical control points located within the interior regions of the local toolpath cells is identified and denoted by $\{\mathbf{p}_i\}_{i=1}^{N_p}$. These points, shown as hollow black markers in Figure 9, represent locations most susceptible to local geometric violations during optimization. For each selected point $\mathbf{p}_i$, a corresponding polygonal admissible region Γ_i is constructed from the surrounding neighboring toolpath segments. This polygon defines the feasible geometric domain within which the associated control point is permitted to move. The admissible polygons associated with representative local toolpath cells are highlighted in red in Figures 9b–9e. Dashed red lines in the figures indicate portions of the polygonal boundary Γ_i that do not coincide with the physical toolpath geometry.

The proposed constraint requires each critical point to remain inside its associated admissible polygon while maintaining a prescribed minimum distance from all polygon edges. This formulation ensures that neighboring toolpaths maintain sufficient separation throughout the optimization process, thereby preventing local intersections and clearance violations. This geometric constraint is mathematically formulated by evaluating the signed distance from each critical point $\mathbf{p}_i$ to its corresponding polygonal admissible region Γ_i. For each point, the distance is computed with respect to all polygon boundary segments that align with the toolpath geometry, and the minimum distance is approximated using a differentiable p-norm aggregation.

For a given point $\mathbf{p}_i$, the distance to the j-th boundary segment $s_{i,j}$ of polygon Γ_i is defined as

$$d_{i,j} = \mathrm{dist}(\mathbf{p}_i,\, s_{i,j}), \tag{21}$$

where $\mathrm{dist}(\mathbf{p}_i, s_{i,j})$ denotes the minimum Euclidean distance between point $\mathbf{p}_i$ and the finite line segment $s_{i,j}$. The minimum distance from point $\mathbf{p}_i$ to polygon Γ_i is approximated using a differentiable p-norm aggregation over all N_s boundary segments of Γ_i,

$$d_i^{\min} \approx \left(\sum_{j=1}^{N_s} d_{i,j}^{-p_c} \right)^{-1/p_c}, \tag{22}$$

where N_s is the total number of boundary segments of Γ_i, and p_c controls the sharpness of the minimum-distance approximation. To distinguish feasible and infeasible configurations, a signed convention is adopted. If point $\mathbf{p}_i$ lies inside its admissible polygon Γ_i, the aggregated distance $d_i^{\min}$ is assigned a positive sign. If the point lies outside, the sign is reversed, yielding a negative value. Accordingly, the signed clearance measure is expressed as

$$\tilde{d}_i = \begin{cases} d_i^{\min}, & \mathbf{p}_i \in \Gamma_i, \\ -d_i^{\min}, & \mathbf{p}_i \notin \Gamma_i. \end{cases} \tag{23}$$

This signed formulation provides a unified measure of geometric feasibility. Positive values above a prescribed threshold correspond to admissible toolpath configurations with sufficient clearance, whereas negative values indicate boundary violation. Enforcing a lower bound on the signed distance measure ensures manufacturable spacing while keeping all critical points inside their corresponding polygonal admissible regions. Although the sign assignment introduces local discontinuities when a point crosses the polygon boundary, its influence on optimization stability was found to be negligible. Such sign transitions might occur only near active constraint boundaries and are further suppressed by the move limits imposed on the design variables, making sign changes infrequent. Moreover, the underlying distance field remains smooth due to the differentiable p-norm aggregation.

Having obtained the signed distance $\tilde{d}_i$ for each critical point $\mathbf{p}_i$, the purpose of the constraint is to enforce

$$\tilde{d}_i \geq d^*, \tag{24}$$

where d^* denotes the prescribed minimum allowable clearance. In the present work, it is selected as $d^* = t_w \alpha$, where t_w is the toolpath width and α is the prescribed spacing ratio between adjacent filaments. This choice corresponds to an overlap ratio of $1 - \alpha$ between neighboring toolpaths. The resulting constraint ensures that every critical point remains sufficiently far from its associated polygon boundary, thereby preventing local intersections while maintaining the prescribed manufacturable spacing between adjacent toolpaths.

The pointwise clearance constraints are combined into a single global differentiable constraint using a soft-min aggregation over all critical points to approximate the minimum signed clearance,

$$\tilde{d}_{\min} = -\frac{1}{\beta_d} \log \left(\sum_{i=1}^{N_p} e^{-\beta_d \tilde{d}_i} \right), \qquad \tilde{d}_{\min} \geq d^*, \tag{25}$$

where $\beta_d > 0$ controls the sharpness of the global minimum approximation. The soft-min formulation is particularly suitable here because the signed distances may contain both positive and negative values, whereas standard p-norm minimum approximations are not directly suited for mixed-sign quantities.

4.1.2 Fixed void regions

In structural design, predefined void regions are often required to accommodate building services and infrastructure systems. Such openings commonly appear in walls, columns, slabs, and beams and must remain free of material throughout the optimization process. To account for this requirement, a fixed-void constraint is introduced to prevent the optimized toolpath from entering prescribed material-free regions of the design domain.

The prescribed void region is represented by a piecewise-linear polygon, denoted by Γ_{void}. In the implementation considered in this work, without loss of generality, the void region is assigned to a selected rhombic cell domain, denoted by Ω_{cell}, within which the opening is located, as illustrated in Figure 10. To ensure that the prescribed void region remains free of deposited material, the toolpath centerline is required to remain outside the void region and maintain a minimum clearance of $t_w/2$ from its boundary. Consequently, the deposited filament of width t_w remains entirely outside the prescribed void region.

A formulation analogous to the clearance and non-intersection constraint described in Section 4.1.1 is employed. Let $\{\mathbf{q}_i\}_{i=1}^{N_v}$ denote the vertices of the prescribed void polygon Γ_{void}. The objective is to ensure that each vertex of Γ_{void} remains outside Ω_{cell} while maintaining a minimum clearance of $t_w/2$ from its boundary. The minimum distance from each point $\mathbf{q}_i$ to the boundary of Ω_{cell} is approximated using the differentiable p-norm formulation given in Eq. (22). A signed distance convention is adopted such that points located outside Ω_{cell} are assigned positive distances, whereas points located inside

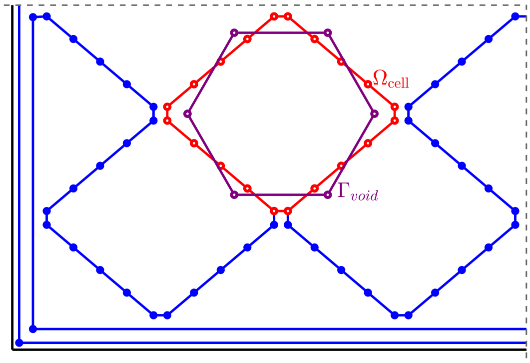

Fig. 10: A prescribed void region Γ_{void} located within the rhombic cell domain Ω_{cell}.

Ω_{cell} are assigned negative distances. The resulting signed distances are then combined using the soft-min aggregation defined in Eq. (25), yielding the global signed void-clearance measure $\tilde{d}^{\text{fv}}_{\min}$. The fixed-void constraint is enforced as

$$\tilde{d}^{\text{fv}}_{\min} \geq \frac{t_w}{2}. \tag{26}$$

Satisfying this constraint guarantees that the prescribed opening remains completely free of material in the optimized design.

4.1.3 Angular regularization constraints

To prevent excessively sharp geometric transitions between neighboring toolpath segments, lower and upper bounds are imposed on the interior angles formed by consecutive control-polygon segments. The angle at each interior control point is computed as

$$\theta_i = \arccos\left(\frac{(\mathbf{P}_{i+1}-\mathbf{P}_i)\cdot(\mathbf{P}_{i-1}-\mathbf{P}_i)}{\|\mathbf{P}_{i+1}-\mathbf{P}_i\|\,\|\mathbf{P}_{i-1}-\mathbf{P}_i\|}\right), \tag{27}$$

for $i = 2, \ldots, N_{\text{cp}}-1$, where N_{cp} is the total number of control points along the toolpath. Smooth p-norm aggregations are employed to approximate the minimum and maximum interior angles,

$$\tilde{\theta}_{\min} \approx \left(\sum_{i=2}^{N_{\text{cp}}-1} \theta_i^{-p_\theta}\right)^{-1/p_\theta}, \qquad \tilde{\theta}_{\max} \approx \left(\sum_{i=2}^{N_{\text{cp}}-1} \theta_i^{p_\theta}\right)^{1/p_\theta}, \tag{28}$$

where p_θ controls the sharpness of the approximation. The angular constraints are then imposed as

$$\tilde{\theta}_{\min} \geq \theta^*_{\min}, \qquad \tilde{\theta}_{\max} \leq \theta^*_{\max}, \tag{29}$$

where $\theta^*_{\min}$ and $\theta^*_{\max}$ denote the prescribed lower and upper angle limits, respectively. These constraints prevent excessively sharp turns and nearly collinear segment configurations, thereby promoting smooth and manufacturable toolpath geometries.

4.2 Sensitivity Analysis

The sensitivities of all objective and constraint functions with respect to the shape design variables $\mathbf{X}$ are evaluated analytically using the chain rule, with adjoint formulations employed for the state-dependent functionals. The mechanical and thermal responses depend on the toolpath geometry through the distance-based density embedding, following the sequence

$$\mathbf{X} \to d_i \to \rho_i \to \bar{\rho}_i \to \{E_i, k_i\} \to \{C, U\}. \tag{30}$$

Accordingly, for a functional f, such as the mechanical compliance or thermal transmittance, the derivative with respect to a scalar design variable x is written as

$$\frac{\partial f}{\partial x} = \sum_{i=1}^{N_e} \frac{\partial f}{\partial \bar{\rho}_i}\frac{\partial \bar{\rho}_i}{\partial \rho_i}\frac{\partial \rho_i}{\partial d_i}\frac{\partial d_i}{\partial x}, \tag{31}$$

where N_e is the number of finite elements. The derivatives of the super-Gaussian filter, the smoothed Heaviside projection, and the RAMP interpolation functions are obtained directly from Eqs. (2), (4), (7), and (16). The derivative of the distance field is evaluated with respect to the active closest toolpath segment associated with each element centroid.

For the mechanical compliance, the stiffness matrix depends on the design variables through the interpolated elastic moduli. Assuming design-independent external loads, differentiation of the equilibrium equations and application of the adjoint method yield a self-adjoint problem, and for multiple load cases the sensitivity is given by

$$\frac{\partial C}{\partial x} = -\sum_{i=1}^{N_L} w_i \mathbf{u}_i^T \frac{\partial \mathbf{K}_m}{\partial x} \mathbf{u}_i, \tag{32}$$

where the derivative $\partial \mathbf{K}_m / \partial x$ is assembled element-wise by differentiating the RAMP interpolation and the density-embedding relation in Eq. (31).

The sensitivity of the thermal transmittance is evaluated in an analogous manner. The thermal state satisfies

$$\mathbf{K}_t \mathbf{T} = \mathbf{F}_t. \tag{33}$$

Introducing the thermal adjoint vector $\boldsymbol{\lambda}$, defined by

$$\mathbf{K}_t^T \boldsymbol{\lambda} = \frac{\partial U}{\partial \mathbf{T}}, \tag{34}$$

the total derivative of the thermal transmittance is

$$\frac{\partial U}{\partial x} = \left.\frac{\partial U}{\partial x}\right|_{\mathbf{T}} + \boldsymbol{\lambda}^T \left(\frac{\partial \mathbf{F}_t}{\partial x} - \frac{\partial \mathbf{K}_t}{\partial x} \mathbf{T} \right). \tag{35}$$

In the present formulation, the convective boundaries and ambient temperatures are fixed with respect to the design variables. Hence, the explicit derivative of U and the derivative of $\mathbf{F}_t$ vanish, and Eq. (35) reduces to

$$\frac{\partial U}{\partial x} = -\boldsymbol{\lambda}^T \frac{\partial \mathbf{K}_t}{\partial x} \mathbf{T}. \tag{36}$$

As above, the derivative $\partial \mathbf{K}_t / \partial x$ is assembled element-wise by differentiating the thermal RAMP interpolation and the density-embedding relation.

The sensitivities of the geometric regularization constraints are evaluated directly from their explicit dependence on the toolpath control-point coordinates. In particular, the clearance, non-intersection, and fixed-void constraints are differentiated through the corresponding point-to-segment distance measures, p-norm approximations, and soft-min aggregations. The angular regularization constraints are differentiated by applying the chain rule to the interior-angle definition and the associated p-norm aggregation functions. The sign convention used in the signed-distance constraints is kept fixed during each sensitivity evaluation.

All objective and constraint sensitivities are therefore obtained analytically with respect to the shape design variables and supplied to the gradient-based optimizer to determine the design update at each iteration.

5 Case studies

In this section, we present a series of examples to demonstrate the efficacy of the proposed framework. While the direct design parameterization of the toolpath and the optimization approach are generic—hence, the framework can be utilized for various applications involving extruder-based additive manufacturing—we focus herein on examples from the construction industry, namely masonry blocks, walls, and beam structures. Accordingly, the toolpath consists of a cementitious material with properties that resemble plain concrete.

For mechanical analysis, the deposited material is assumed linear elastic with a Young's modulus of $E = 30{,}000$ MPa and a Poisson's ratio of $\nu = 0.25$. A minimum stiffness of $E_{\min} = 10^{-3}$ MPa is employed to avoid singularities in the finite element analysis with a fixed grid. For thermal analysis, heat transfer is driven by prescribed ambient temperatures of $T_{\text{out}} = 1$ and $T_{\text{in}} = 0$, representing normalized outdoor and indoor temperatures, respectively. This normalization affects only the temperature scale and does not alter the optimization procedure or the resulting optimal geometries.

Convective boundary conditions are imposed using heat transfer coefficients of $h_{co} = 25$ W/(m^{2}K) for the exterior surface and $h_{ci} = 7.7$ W/(m^{2}K) for the interior surface, following the values suggested by Sousa et al. (2011). The remaining boundaries are assumed to be adiabatic, with zero heat flux. The thermal conductivities of the solid and void phases are taken as $k_{\max} = 0.7$ W/(m K) and $k_{\min} = 0.05$ W/(m K), respectively.

Optimization is performed using MMA (Svanberg 1987). The RAMP penalization parameters in Eqs. (7) and (16) are set to $q_m = q_t = 3$, while the super-Gaussian filter exponent p_f in Eq. (2) is fixed at 6. A continuation scheme is applied to the sharpness parameter β_{HV} in Eq. (4), the soft-min parameter β_d in Eq. (25), the angular aggregation parameter p_θ in Eq. (28), and the clearance aggregation parameter p_c in Eq. (22). These parameters are initialized at 4 and doubled every 20 optimization iterations until a maximum value of 16 is reached. To ensure that all continuation parameters reach their prescribed maximum values and remain at these values for at least 10 iterations, a minimum of 50 optimization iterations is enforced, while a maximum of 120 iterations is allowed. After the minimum iteration count is reached, convergence is declared when the maximum relative change in the objective function and active constraint values over three consecutive iterations falls below 10^{-3}. The move limits of the shape design variables are specified separately for each example according to the problem dimensions. The lower and upper bounds are selected to ensure that the optimized toolpath remains within the inner perimeter layer while maintaining a minimum spacing of αt_w between neighboring filaments.

To improve numerical scaling, the compliance and thermal transmittance values that appear in the objective and constraint functionals are normalized by their corresponding values, evaluated for the initial design configuration using the final values of the continuation parameters. The angular bounds in Eq. (29) are prescribed as $\theta^*_{\min} = \pi/4$ and $\theta^*_{\max} = 2\pi - \theta^*_{\min}$.

In the following figures, the toolpaths' center lines are shown in green, with the control points indicated by green markers, to provide clear visual contrast with the grayscale density field.

5.1 Cross-section design of a masonry block

This case study demonstrates the application of the proposed framework to the design of masonry block cross-sections with manufacturable internal toolpath layouts, while addressing both structural and thermal performance requirements.

Square and rectangular masonry block geometries with different infill configurations are considered. The corresponding mechanical and thermal boundary conditions are illustrated in Figure 11. For the mechanical performance, two self-equilibrated load cases are considered: (i) Uniform compressive traction $t_x = 1$ kN/m applied to the two faces corresponding to the interfaces between adjacent blocks (load case 1); (ii) Uniform compressive traction $t_y = 1$ kN/m applied to the indoor and outdoor faces of the block (load case 2). While masonry blocks are not necessarily designed for load bearing (this depends on specific local practices and design provisions), we apply these load cases to enforce a certain stiffness requirement that has a trade-off with thermal performance, such that non-trivial optimized designs can emerge. Equal weighting factors of $w_1 = w_2 = 0.5$ are assigned to the two load cases.

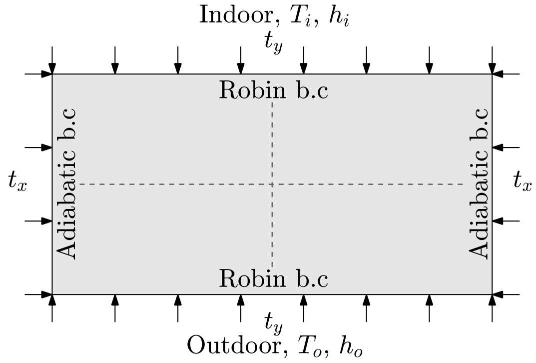

Fig. 11: Mechanical and thermal boundary conditions for the masonry block case study. Dashed lines denote symmetry axes.

By exploiting geometric and boundary-condition symmetries, the computational domain is reduced accordingly. For the mechanical analysis and optimization, only the bottom-left quarter of the full domain is considered, with symmetry boundary conditions imposed along the symmetry axes. The full block cross-section is subsequently reconstructed through mirroring. For the thermal analysis, only the left half of the domain is considered, with a symmetry boundary condition imposed along the vertical symmetry axis.

The first set of examples considers a square masonry block of dimensions 0.4×0.4 m with a prescribed toolpath width of $t_w = 0.01$ m. The design domain is discretized using finite elements of size $t_w/10 = 0.001$ m. The move limit of the design variables is set to $t_w/4 = 0.0025$ m. The masonry block geometry is optimized using the three optimization formulations introduced in Section 4. In the third formulation, corresponding to compliance minimization subject to a thermal transmittance constraint, the thermal transmittance is constrained to at most 98% of its initial value. The rationale for selecting this threshold is discussed later in this section. Furthermore, for the diagonally symmetric square-block examples, Formulation #1 was solved with a diagonal symmetry regularization to remove a small bias introduced by the toolpath parametrization. Additional details are provided in A.

Two toolpath configurations are considered, as summarized in Table 1. In all cases, the toolpath consists of two perimeter layers, while the infill pattern varies according to the selected configuration.

Configuration	N_{rx}	N_{ry}	N_{seg}	N_{o}
#1	3	3	3	2
#2	5	5	3	2

Table 1: Toolpath configurations considered for the square masonry block case study.

The corresponding initial and optimized designs for the 3×3 and 5×5 toolpath configurations are shown in Figures 12 and 13, respectively. For each configuration, results are presented for all three optimization formulations. The corresponding mean compliance of the two load cases and the thermal transmittance values are summarized in Table 2. Owing to the symmetry of the square block and the applied loading, both load cases yield identical compliance values. Interestingly, the results indicate that the three optimization formulations lead to distinctly different infill toolpath geometries, especially when comparing Formulation #1 (structural compliance only) versus Formulation #2 (thermal transmittance).

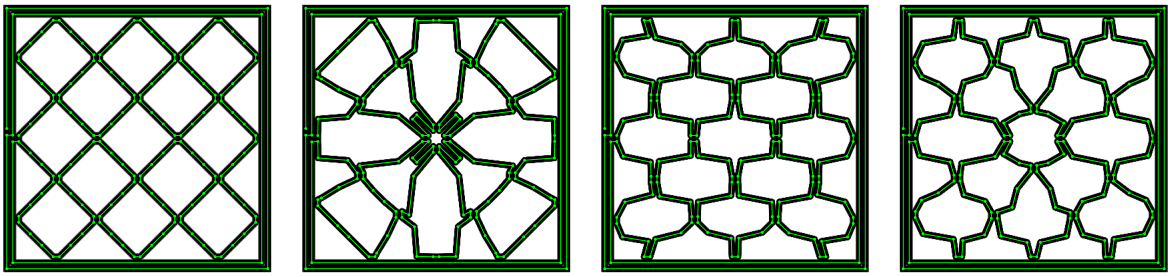

(a) Initial (b) Formulation 1 (c) Formulation 2 (d) Formulation 3

Fig. 12: Optimization results for the block configuration $N_{\mathrm{rx}} = 3$, $N_{\mathrm{ry}} = 3$, and $N_{\mathrm{seg}} = 3$.

As expected, Formulation #1 consistently yields the stiffest designs, while Formulation #2 consistently yields the lowest thermal transmittance. In some cases, e.g., Configuration #1 and Formulation #2, compliance is reduced alongside transmittance, despite not being considered in the optimization. This is not expected in general, as demonstrated by the results of Configuration #2 and Formulation #2, where compliance is compromised.

From a geometric perspective, for improving thermal insulation, the optimization transforms the initial symmetric rhombus lattice into a horizontally elongated cellular morphology. The large four-way junctions are replaced by narrower, staggered connections, reducing the continuity of conductive

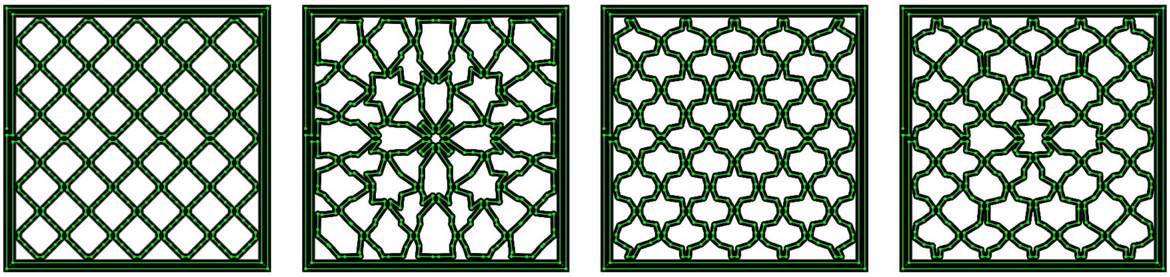

(a) Initial (b) Formulation 1 (c) Formulation 2 (d) Formulation 3

Fig. 13: Optimization results for the block configuration $N_{\mathrm{rx}} = 5$, $N_{\mathrm{ry}} = 5$, and $N_{\mathrm{seg}} = 3$.

Configuration	Formulation	Compliance ($\times 10^3$) [N m]		Transmittance [W/m^2]	
		Initial	Optimized	Initial	Optimized
#1	#1	0.175	0.015 (8.69%)	0.447	0.471 (105.33%)
	#2	0.175	0.081 (46.17%)	0.447	0.434 (96.99%)
	#3	0.175	0.080 (45.46%)	0.447	0.440 (98.34%)
#2	#1	0.044	0.010 (23.52%)	0.570	0.607 (106.52%)
	#2	0.044	0.044 (101.26%)	0.570	0.557 (97.77%)
	#3	0.044	0.027 (62.90%)	0.570	0.560 (98.28%)

Table 2: Initial and optimized compliance and thermal transmittance values for the square masonry block case study. Percentages indicate optimized values relative to the initial design. Formulations #1–#3 correspond to compliance minimization, thermal transmittance minimization, and compliance minimization with a thermal constraint.

paths through the solid phase. Simultaneously, the elongation of the cavities perpendicular to the imposed vertical heat flow increases the extent of the low-conductivity regions that obstruct heat transfer, thereby reducing the thermal transmittance. A noteworthy feature of the parameterization is its natural capability to obtain manufacturable designs containing multiple adjacent toolpaths, even if those were not present in the initial design. Some examples are the congestion of four parallel segments in the center of the design in Figure 12b and the doubled vertical segments in Figures 12c and 12d. This highlights an important advantage of directly optimizing the toolpath, whereas indirectly optimizing the topology and shape of the infill and subsequently interpreting it as a toolpath will pose a difficulty because a discrete number of parallel passes needs to be enforced. This challenging aspect was recently approached by Kim-Tackowiak et al. (2026) using mixed-integer programming, at the expense of limiting the designs to prescribed ground structures.

The numerical results show that the achievable variation in thermal transmittance remains within only a few percent of the initial value. This indicates that the considered toolpath parameterization provides substantially greater freedom for modifying the structural stiffness than the thermal performance. The limited improvement in thermal transmittance is consistent with the fact that the initial cellular layouts already exhibit characteristics of foam-like insulating structures, which are known to provide efficient thermal resistance through a distributed network of enclosed voids. Consequently, the solutions obtained using Formulation #2 may be viewed as near-optimal thermal designs within the prescribed design space, suggesting that only modest further reductions in thermal transmittance are possible through geometric modifications alone. From a practical perspective, alternative toolpath topologies may first be evaluated to identify a suitable thermal baseline, which can be subsequently improved by employing Formulations #2 or #3.

All optimization runs converged shortly after the minimum prescribed number of 50 iterations, requiring only an additional 3 to 4 iterations to satisfy the convergence criterion. The convergence history for Configuration #1 under Formulation #3, whose optimized design is shown in Figure 12d, is presented in Figure 14 as a representative example. The optimization terminated after 53 iterations, with smooth objective and constraint histories indicating stable convergence of the solution process. The resulting thermal transmittance is 98.34% of the initial value, compared to the prescribed limit

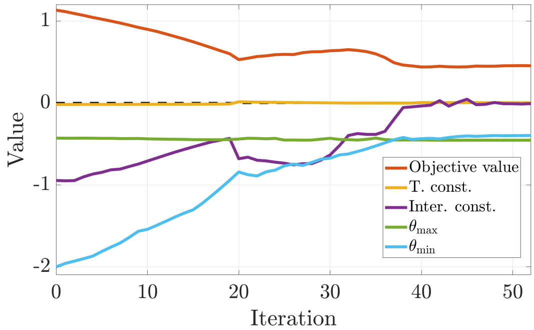

Fig. 14: Convergence history for Configuration #1 of the square masonry block case study under Formulation #3. The optimization converged after 53 iterations.

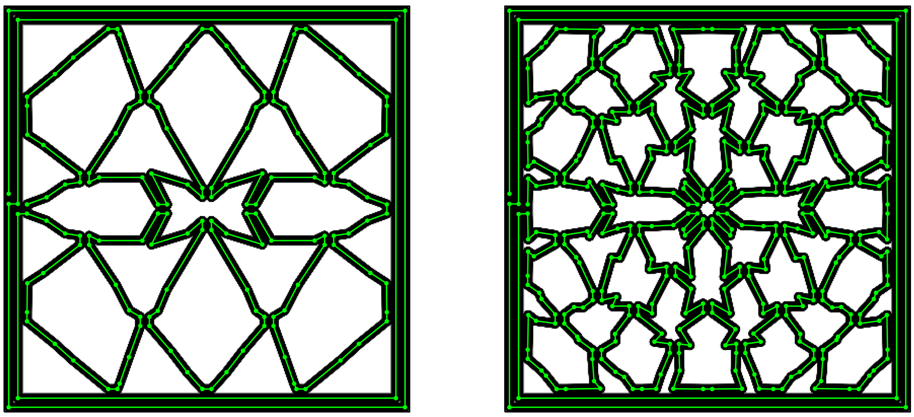

(a) $N_{rx} = N_{ry} = 3,\ N_{seg} = 3$

(b) $N_{rx} = N_{ry} = 5,\ N_{seg} = 3$

Fig. 15: Optimized designs obtained using Formulation #1 without enforcing diagonal symmetry. Structural improvements are distributed unevenly between the two loading conditions, leading to non-diagonally symmetric solutions.

of 98%. For reference, Formulation #2 applied to the same configuration achieved a transmittance of 96.99%. This indicates that lower thermal transmittance values are attainable within the current parameterization and that the optimization procedure could, if desired, enforce the thermal constraint more aggressively. The angular regularization constraints remained inactive for this particular optimization run; however, they became active in other optimization cases considered in this study. In contrast, the intersection constraint became active in the final design, indicating that in certain regions neighboring toolpath filaments approached the prescribed minimum allowable spacing.

To illustrate the influence of the adopted diagonal symmetry regularization, both configurations were re-optimized using Formulation #1 without enforcing diagonal symmetry. The resulting designs are shown in Figure 15. In this case, the optimizer identified configurations in which the compliance reduction is no longer distributed equally between the two loading conditions, as would be expected in an ideally symmetric setting. Instead, the optimization prioritized the structural improvement in one loading condition more than the other, resulting in non-diagonally symmetric designs.

To further investigate the influence of the block geometry, the proposed framework is applied to a rectangular masonry block of dimensions 0.8×0.4 m. The toolpath configuration consists of $N_{rx} = 6$, $N_{ry} = 3$, and $N_{seg} = 3$. The corresponding initial and optimized designs obtained for the three optimization formulations are shown in Figure 16. The corresponding compliance and thermal transmittance ratios, expressed as percentages relative to the initial design, are summarized in Table 3.

The results for the rectangular configuration reveal a stronger trade-off between structural and thermal performance than that observed for the square blocks. This can be seen, for example, in the results of Formulation #2 where the compliance of the second load case is strongly affected because the load is applied parallel to the heat-flow direction.

Notably, across all examples presented in this case study, the thermally optimized designs obtained using Formulation #2 exhibit a consistent tendency toward larger and more uniform void regions.

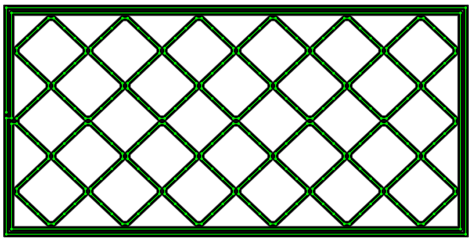

(a) Initial design

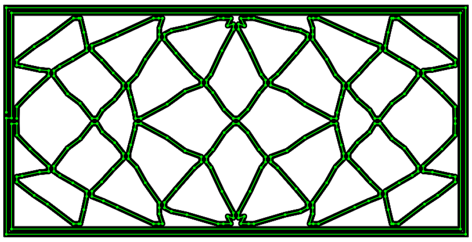

(b) Formulation #1
Min. compliance

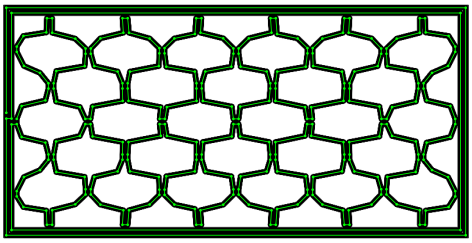

(c) Formulation #2
Min. transmittance

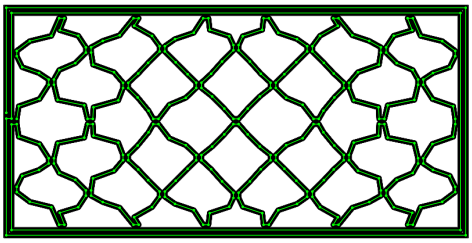

(d) Formulation #3
Combined

Fig. 16: Initial and optimized designs for the rectangular masonry block with $N_{\mathrm{rx}} = 6$, $N_{\mathrm{ry}} = 3$, and $N_{\mathrm{seg}} = 3$.

Formulation	Compliance (% of initial)			Transmittance (% of initial)
	Load case 1	Load case 2	Combined	
#1	49.95%	47.20%	48.57%	102.22%
#2	149.44%	434.00%	291.72%	96.95%
#3	99.87%	141.18%	120.52%	98.55%

Table 3: Optimization of a rectangular masonry block. Optimized compliance for the two load cases, the combined compliance measure, and thermal transmittance, are expressed as percentages relative to the initial design. Formulations #1–#3 correspond to compliance minimization, thermal transmittance minimization, and compliance minimization with a thermal constraint.

In contrast, the designs obtained using Formulation #1 develop pronounced load-carrying features that enhance structural stiffness. The mixed formulation (Formulation #3) combines characteristics of both solutions, preserving the main load-carrying features of the compliance-optimal design while retaining several geometric characteristics of the thermally optimized design, including enlarged void regions. Consequently, the resulting geometries provide a compromise between structural and thermal performance.

To further improve the achievable thermal performance, the toolpath parameterization can be relaxed by allowing selected connections within the rhombic cells to be disconnected, thereby increasing the geometric design freedom. This relaxed parameterization is investigated for the two case studies summarized in Table 4. Each case study is solved using the three optimization formulations presented in Section 4. In the combined formulation, the thermal transmittance is constrained to be at most 90% of its initial value while minimizing the structural compliance. The disconnections are introduced along the horizontal toolpath connections located at the mid-height of the block. This location is selected because it directly interrupts the dominant heat-conduction path between the indoor and outdoor faces while preserving continuous load-transfer paths along the perimeter, thereby providing additional design freedom for improving thermal performance.

Figures 17 and 18, together with the quantitative results reported in Table 5, illustrate the additional design flexibility provided by the relaxed parameterization. The candidate disconnection

Configuration	L_x [m]	L_y [m]	N_{rx}	N_{ry}	N_{seg}	N_{o}
#1 – Square	0.4	0.4	5	5	2	2
#2 – Rectangular	0.8	0.4	6	3	2	2

Table 4: Toolpath configurations considered for the relaxed parameterization.

locations are indicated by the blue circles in the initial designs. Compared with the fully connected parameterization, the optimizer exploits these potential disconnections to interrupt the conductive heat path more effectively. As expected, Formulation #1 preserves all of the horizontal connections, because maintaining a continuous load-transfer path is beneficial for structural stiffness. Consequently, this formulation achieves the largest reduction in compliance while slightly increasing the thermal transmittance.

In contrast, Formulation #2 prioritizes thermal insulation by disconnecting the toolpath at the selected locations, thereby creating a pronounced separation between the upper and lower portions of the block. This significantly reduces the thermal transmittance by interrupting the dominant heat-conduction path, at the expense of structural stiffness. As expected, Formulation #3 provides a compromise between the competing mechanical and thermal objectives. The two mechanical load cases also reveal the directional dependence of the optimized layouts. As expected, load case 2 is more sensitive to the horizontal disconnections because the load is applied in the same direction as the heat-flow path.

In summary, these results demonstrate that introducing controlled toolpath disconnections increases the geometric design freedom, enabling substantially greater reductions in thermal transmittance while maintaining structurally efficient and manufacturable toolpath layouts. By deliberately choosing specific disconnections, users of the method are able to drive the design towards desirable outcomes, such as optimized void regions for thermal insulation.

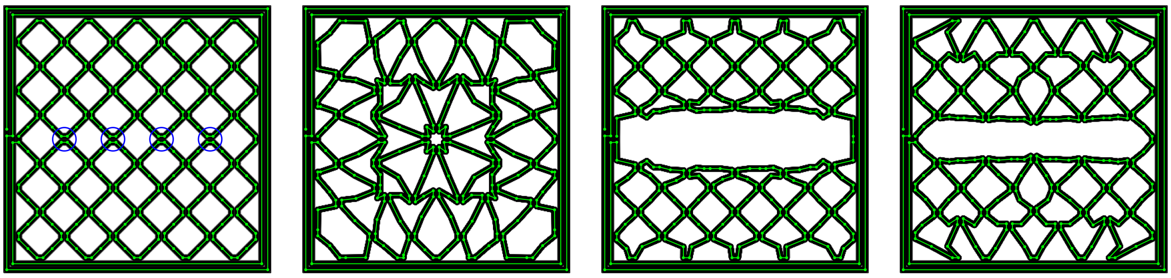

(a) Initial design (b) Formulation #1 Min. compliance (c) Formulation #2 Min. transmittance (d) Formulation #3 Combined

Fig. 17: Initial and optimized toolpath layouts for a square block using the relaxed parameterization with disconnected rhombic cells.

5.2 Cross-section design of a wall segment

This case study demonstrates the applicability of the proposed formulation to the cross-sectional design of walls. Owing to the repetitive nature of walls and their typical loading conditions, the model is defined as a periodic wall segment rather than as a full wall.

The periodic wall segment has dimensions $L_x \times L_y$, where L_x denotes the length of the periodic cell and L_y the wall thickness. The wall thickness is fixed at $L_y = 0.4$ m, while the periodic cell length is $L_x = 0.2$ m. The corresponding boundary conditions are illustrated in Figure 19. The thermal boundary conditions are identical to those used in the masonry block case study. For the mechanical analysis, a self-equilibrated compressive traction of $t_y = 1$ kN/m is applied to the indoor and outdoor faces of the periodic segment, while periodic boundary conditions are imposed on the remaining vertical faces to ensure continuity between adjacent unit cells. Owing to the symmetry of both the geometry and the loading, only one quarter of the periodic cell is optimized. The complete

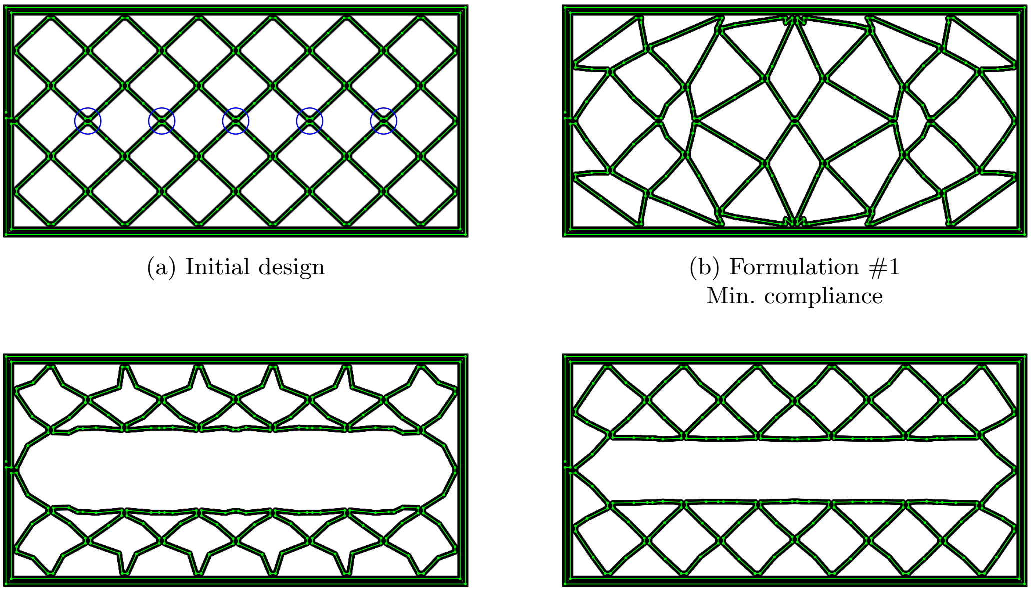

(a) Initial design

(b) Formulation #1
Min. compliance

(c) Formulation #2
Min. transmittance

(d) Formulation #3
Combined

Fig. 18: Initial and optimized toolpath layouts for a rectangular block using the relaxed parameterization with disconnected rhombic cells.

Configuration	Formulation	Compliance (% of initial)			Transmittance (% of initial)
		Load case 1	Load case 2	Combined	
#1 – Square	#1	26.19%	26.72%	26.45%	104.65%
	#2	38.06%	68.64%	53.35%	83.26%
	#3	32.77%	61.13%	46.95%	88.74%
#2 – Rectangular	#1	54.27%	45.57%	49.92%	102.81%
	#2	98.28%	706.82%	402.55%	79.17%
	#3	53.84%	362.12%	207.98%	83.45%

Table 5: Optimized compliance for the two load cases, the combined compliance measure, and thermal transmittance, expressed as percentages relative to the initial design. Formulations #1–#3 correspond to compliance minimization, thermal transmittance minimization, and compliance minimization with a thermal constraint.

periodic unit cell is subsequently reconstructed by mirroring the optimized quarter, and the full wall geometry is obtained by periodically repeating the resulting unit cell.

The periodic nature of the model implies that a single rhombic cell should be defined in the horizontal direction ($N_{rx} = 1$). Three configurations are considered in the vertical direction, with $N_{ry} = 1$, 2, and 3, to investigate the influence of the wall topology on the optimized toolpath layout and the resulting thermo-mechanical performance. Since the left and right boundaries are periodic, perimeter layers are required only along the top and bottom boundaries, and two perimeter layers are employed ($N_o = 2$). Each edge of the rhombic cell is discretized into three segments ($N_{\text{seg}} = 3$). As in the previous case studies, three optimization formulations are considered: compliance minimization, thermal transmittance minimization, and compliance minimization subject to an upper bound on the thermal transmittance. In the third formulation, the thermal transmittance is constrained to at most 105% of its initial value. This relatively relaxed constraint provides sufficient geometric freedom for the optimizer to significantly improve the structural performance while limiting the degradation in thermal insulation to only 5% relative to the initial design.

The initial and optimized toolpath layouts for a 0.8 m-long wall segment, consisting of four periodically repeated unit cells, are shown in Figure 20. For each wall configuration, results are presented

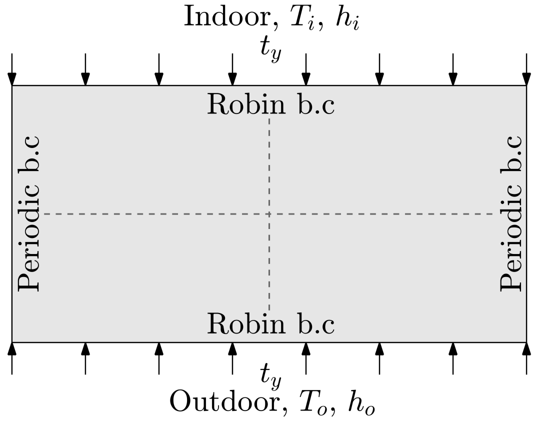

Fig. 19: Mechanical and thermal boundary conditions for the wall case study. Dashed lines denote symmetry axes.

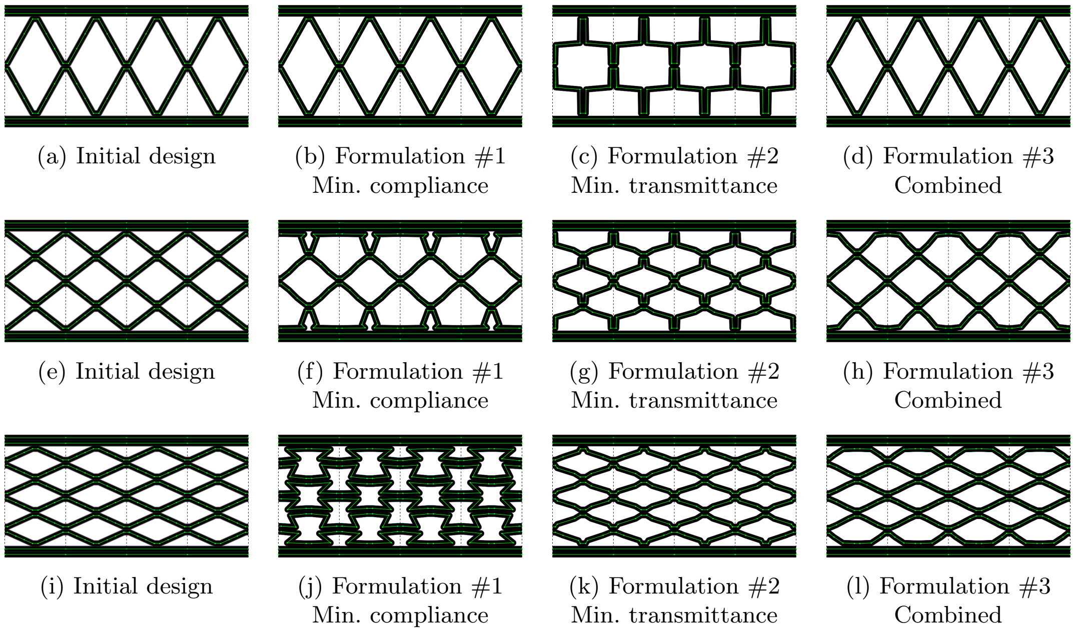

Fig. 20: Initial and optimized toolpath layouts for the three wall configurations. Results are shown for the three optimization formulations: (#1) compliance minimization, (#2) thermal transmittance minimization, and (#3) compliance minimization subject to a thermal transmittance constraint.

for all three optimization formulations. The corresponding compliance and thermal transmittance values are summarized in Table 6.

For Configuration #1, compliance minimization (Formulations #1 and #3) produces virtually no change in the toolpath layout, indicating that the initial design is already close to the optimal structural configuration for the applied loading. Consequently, both the compliance and thermal transmittance remain essentially unchanged. In contrast, thermal transmittance minimization (Formulation #2) modifies the toolpath to increase the separation between the indoor and outdoor faces and interrupt direct heat-conduction paths. This improves the thermal performance, albeit at the expense of a substantial increase in compliance.

For Configuration #2, compliance minimization (Formulation #1) strengthens the vertical load paths by increasing the connectivity between the top and bottom boundary layers, leading to a substantial improvement in structural stiffness but a deterioration in thermal performance due to the formation of more direct heat-conducting paths. In contrast, thermal transmittance minimization (Formulation #2) preserves larger enclosed cavities and interrupts the heat-conduction paths through the wall, improving thermal insulation at the expense of structural stiffness. The balanced

Configuration	Formulation	Compliance ($\times 10^3$) [N m]		Transmittance [W/m^2]	
		Initial	Optimized	Initial	Optimized
#1	#1	0.006	0.006 (100.29%)	0.424	0.423 (99.79%)
	#2	0.006	0.027 (438.53%)	0.424	0.400 (94.23%)
	#3	0.006	0.006 (100.29%)	0.424	0.423 (99.79%)
#2	#1	0.013	0.007 (52.25%)	0.386	0.442 (114.34%)
	#2	0.013	0.025 (198.74%)	0.386	0.375 (97.04%)
	#3	0.013	0.010 (80.41%)	0.386	0.405 (104.88%)
#3	#1	0.030	0.003 (8.64%)	0.369	0.677 (183.49%)
	#2	0.030	0.037 (122.87%)	0.369	0.364 (98.57%)
	#3	0.030	0.021 (71.14%)	0.369	0.387 (104.94%)

Table 6: Initial and optimized compliance and thermal transmittance values for the wall case study. Percentages indicate optimized values relative to the initial design. Configurations #1–#3 correspond to the three wall layouts considered, while Formulations #1–#3 correspond to compliance minimization, thermal transmittance minimization, and compliance minimization with a thermal constraint.

thermo-mechanical optimization (Formulation #3) provides a compromise between these competing responses, improving the structural performance by approximately 20% while maintaining the thermal transmittance within the prescribed limit.

For Configuration #3, the larger number of rhombic cells provides greater geometric flexibility, resulting in the most pronounced differences between the three optimization formulations. Under compliance minimization (Formulation #1), the optimizer transforms the initial lattice into nearly continuous vertical load paths, producing the largest improvement in structural stiffness among the considered configurations, but also a substantial deterioration in thermal performance. In contrast, thermal transmittance minimization (Formulation #2) preserves insulating cavities and interrupts conductive paths through the wall, improving thermal insulation at the expense of structural stiffness. The thermo-mechanical optimization (Formulation #3) again provides a compromise, reducing the compliance by approximately 29% while maintaining the thermal transmittance within the prescribed limit.

Overall, the results demonstrate the applicability of the proposed optimization framework to the design of periodic wall structures. By directly parameterizing the toolpath geometry, an abundance of optimized geometries can be generated, that clearly reflect the objective to be minimized and the constrained responses. Furthermore, the parameterized toolpaths can be communicated to a robotic fabrication facility in a straightforward manner without any need for interpretation.

5.3 Infill design in beams

While the first two case studies were inspired by applications of 3D printing in cementitious materials, the third case aims to demonstrate the general applicability of the method to design scenarios that involve optimization of infill patterns. For this purpose, we focus on compliance minimization of beam structures under various boundary conditions and toolpath configurations. In addition, the application of a material-free region constraint introduced in Section 4.1.2 is illustrated.

All beams considered in this study have dimensions $l_x = 4$ m and $l_y = 0.6$ m, with a prescribed toolpath width of $t_w = 0.04$ m. The design domain is discretized using finite elements of size $t_w/8 = 0.005$ m, and the move limit of the design variables is set to $t_w/4 = 0.01$ m. Two toolpath configurations are considered. The first configuration is defined by $N_{\mathrm{rx}} = 8$ and $N_{\mathrm{ry}} = 1$, while the second is defined by $N_{\mathrm{rx}} = 8$ and $N_{\mathrm{ry}} = 3$. In both configurations, each rhombus edge is discretized into $N_{\mathrm{seg}} = 2$ segments, and the toolpath consists of $N_{\mathrm{o}} = 2$ perimeter layers. Two sets of boundary conditions are investigated. The first corresponds to a cantilever beam clamped along the left edge and subjected to a uniformly distributed load of magnitude 1 kN/m acting on the right edge. The second corresponds to a simply supported beam subjected to a uniformly distributed load of magnitude 1 kN/m applied along the top boundary.

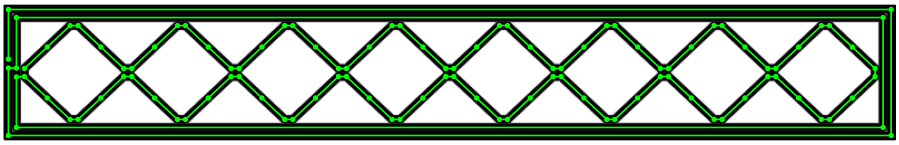

(a) Initial design

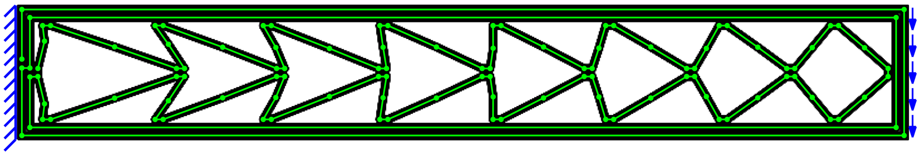

(b) Optimized cantilever beam

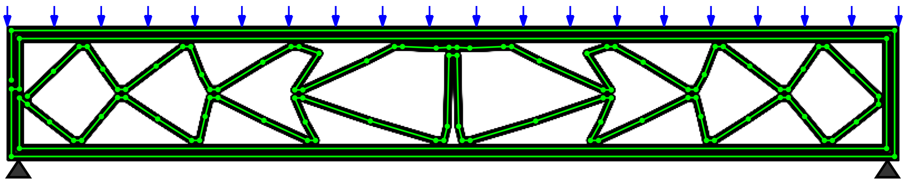

(c) Optimized simply supported beam

Fig. 21: Initial and optimized beam designs for the toolpath configuration $N_{rx} = 8$, $N_{ry} = 1$. The initial design is shown in (a), while (b) and (c) present the optimized cantilever and simply supported beam configurations, respectively.

Configuration	Boundary Condition	Compliance ($\times 10^{-7}$) [N m]	
		Initial	Optimized
$N_{rx} = 8,\ N_{ry} = 1$	Cantilever	0.259	0.237 (91.30%)
	Simply supported	0.346	0.319 (92.22%)
	Simply supported & fixed void	0.346	0.325 (93.78%)
$N_{rx} = 8,\ N_{ry} = 3$	Cantilever	0.223	0.186 (83.40%)
	Simply supported	0.354	0.270 (76.33%)

Table 7: Initial and optimized compliance values for the beam examples. Percentages indicate the optimized compliance relative to the corresponding initial value.

By exploiting geometric and loading symmetries, only half of each beam domain is analyzed. For the cantilever beam, symmetry is imposed with respect to the horizontal mid-height axis, whereas for the simply supported beam, symmetry is imposed with respect to the vertical mid-span axis. The full beam geometries are subsequently reconstructed by mirroring the optimized half-domain solutions. To demonstrate the effectiveness of the proposed material-free region constraint, the simply supported beam corresponding to the toolpath configuration $N_{\mathrm{rx}} = 8$ and $N_{\mathrm{ry}} = 1$ is optimized again after introducing a prescribed fixed void region.

Figures 21 and 22 present the initial and optimized beam designs obtained for the two toolpath configurations considered in this study without a prescribed fixed void region. The corresponding example incorporating a fixed void region is shown in Figure 23, where the prescribed void region, denoted by Γ_{void}, is highlighted by the purple hexagon and the corresponding cell domain Ω_{cell} is marked in red. A detailed view of the enforced fixed void region is provided in Figure 24. In all cases, the optimization converged smoothly while satisfying the prescribed geometric constraints. The corresponding compliance values, together with the optimized values expressed as percentages of the initial compliance, are summarized in Table 7.

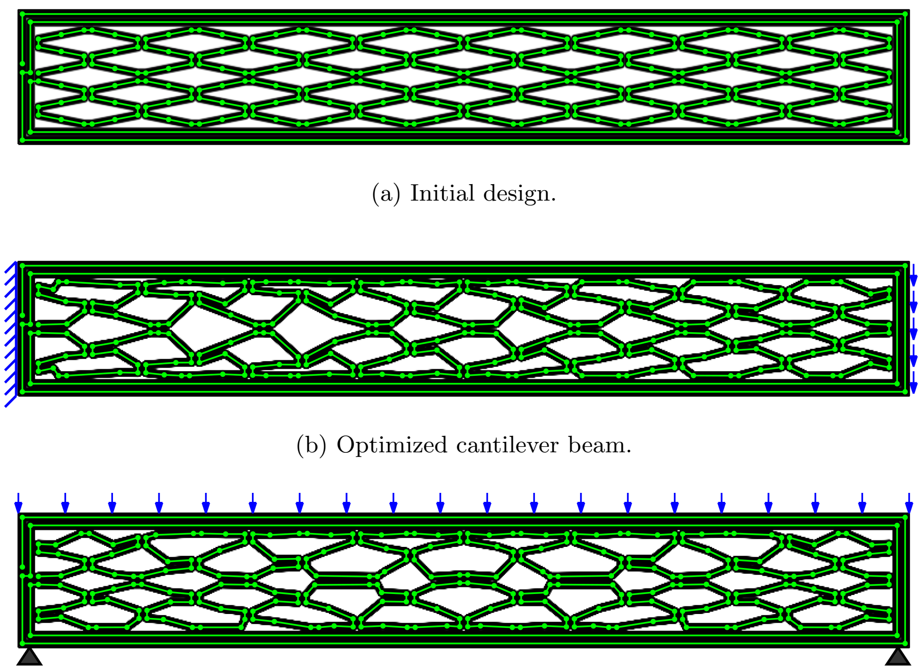

(a) Initial design.

(b) Optimized cantilever beam.

(c) Optimized simply supported beam.

Fig. 22: Initial and optimized beam designs for the toolpath configuration $N_{rx} = 8$, $N_{ry} = 3$. The initial design is shown in (a), while (b) and (c) present the optimized cantilever and simply supported beam configurations, respectively.

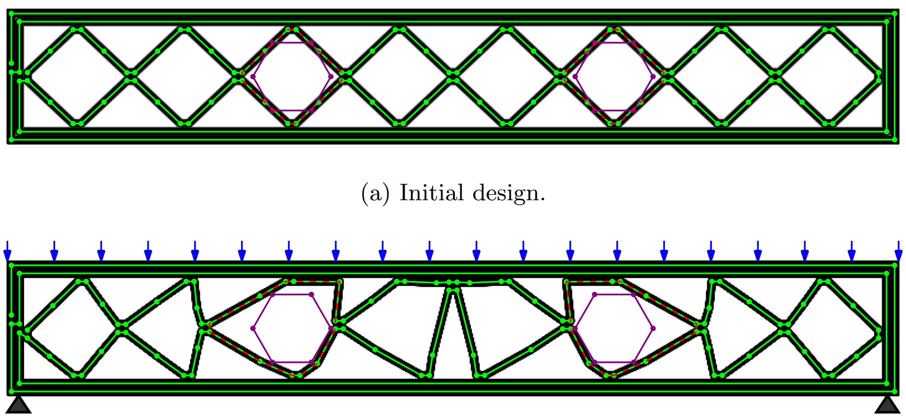

(a) Initial design.

(b) Optimized design.

Fig. 23: Simply supported beam with a prescribed fixed void region for the toolpath configuration $N_{rx} = 8$ and $N_{ry} = 3$. The prescribed void region Γ_{void} is highlighted by the purple hexagon, while the corresponding cell domain Ω_{cell} is marked in red.

Interestingly, we obtain designs that align with well-known results from the field of continuum topology optimization. One example is the design of Figure 21b that resembles optimized bracing patterns in high-rise buildings (e.g., Stromberg et al. 2012). Another example are the designs with relatively dense infill as in Figure 22, that resemble results achieved when a maximum length scale is imposed, e.g., Guest (2009) and Wu et al. (2018).

The results summarized in Table 7 demonstrate that the proposed parameterization is capable of reducing the compliance of beam structures under different loading conditions and when incorporating fixed void regions. For the example with the prescribed fixed void region, Figure 23a shows that

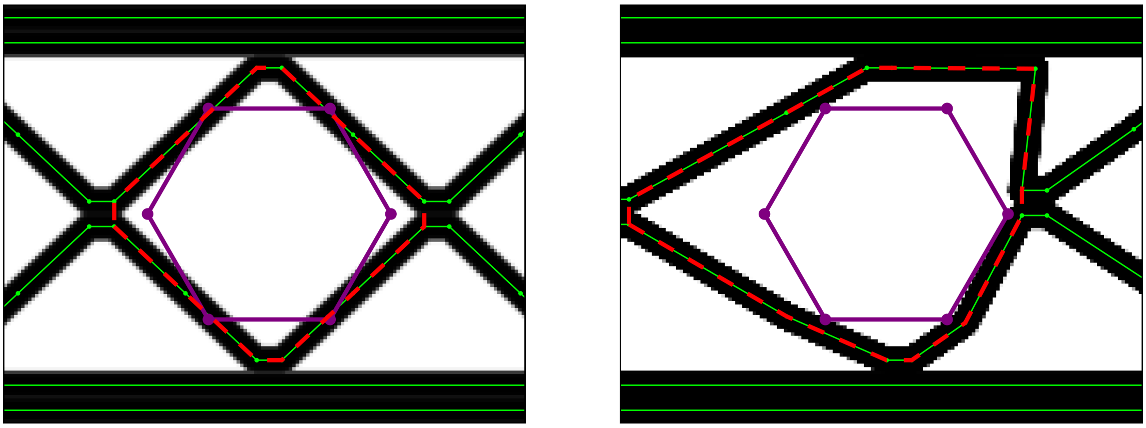

(a) Initial design. (b) Optimized design.

Fig. 24: Detailed view of the prescribed fixed void region. The initial configuration violating the void constraint is shown in (a), while the optimized configuration satisfying the prescribed minimum distance requirement is shown in (b).

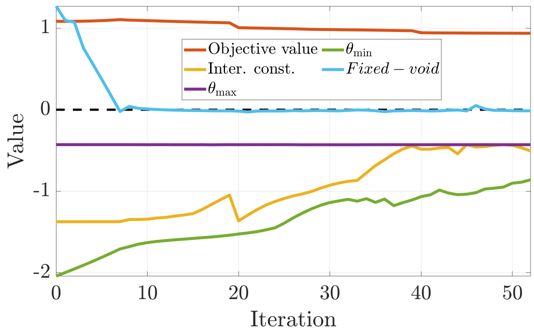

Fig. 25: Convergence history for the simply supported beam with a prescribed fixed void region.

portions of the cell domain Ω_{cell} initially lie inside the void region Γ_{void}, thereby violating the constraint. In the optimized design shown in Figure 23b, the prescribed minimum separation distance of $t_w/2$ from the void boundary is satisfied. Furthermore, several portions of the toolpath approach the admissible limit imposed by Γ_{void}, indicating efficient utilization of the available design space while preserving the material-free region.

The convergence history for the optimization problem with the fixed void region is shown in Figure 25, illustrating smooth and stable convergence throughout the optimization process. The optimization converged after 53 iterations. The blue curve corresponds to the fixed void region constraint, which is initially violated but gradually becomes satisfied during the optimization process.

6 Conclusion

We presented a framework for the direct optimization of continuous, non-intersecting toolpath geometries for fabrication by extruder-based additive manufacturing. In the proposed approach, the printable toolpath serves both as the geometric representation and as the optimization design variables, eliminating the need for intermediate design representations and post-processing results for generating manufacturable toolpaths. The method combines an explicit distance-based embedding technique with differentiable geometric constraints to ensure continuous, manufacturable toolpaths while facilitating finite element-based structural and thermal analyses within a unified optimization framework.

The efficacy of the proposed approach was demonstrated by optimizing cross-section patterns of masonry blocks and walls, as well as infill patterns of beam structures. The numerical results showed the generation of manufacturable toolpath layouts for a range of structural and thermal design objectives, including compliance minimization, thermal transmittance minimization, and their combined optimization. Furthermore, the introduction of a relaxed parameterization with selectively disconnected toolpath segments demonstrated that increasing the geometric design freedom can substantially improve the achievable thermal insulation while maintaining manufacturable designs.

The current work establishes a foundation for direct toolpath-based structural optimization for extrusion-based additive manufacturing. Future work will focus on extending the formulation to fully three-dimensional toolpaths, incorporating additional manufacturing considerations such as process-dependent material behavior, buildability constraints, and multi-material deposition, as well as enabling topological changes through adaptive toolpath connectivity. These developments will further expand the applicability of the proposed method to practical large-scale applications of additive manufacturing.

Acknowledgments. The authors gratefully acknowledge the support of the European Innovation Council.

Statements and Declarations

Funding

This research was supported by the European Union under the project AM2PM: Additive to Predictive Manufacturing for Multistorey Construction Using Learning by Printing and Networked Robotics (HORIZON-EIC-2023-PATHFINDERCHALLENGES-01). The support of the European Innovation Council is gratefully acknowledged.

Competing Interests

The authors have no competing interests to declare.

Author Contributions

Emad Shakur: Conceptualization, Methodology, Software, Investigation, Writing – original draft, Writing – review & editing.
Oded Amir: Conceptualization, Methodology, Software, Investigation, Writing – original draft, Writing – review & editing.

Ethics Approval and Consent to Participate

Not applicable.

Data Availability

The data that support the findings of this study are available from the corresponding author upon reasonable request.

Replication of Results

The results can be reproduced using the methodology and parameters described in the manuscript. All relevant equations, boundary conditions, and key parameters are provided. Interested readers may contact the corresponding author for additional implementation details and supporting materials.

Appendix A Diagonal symmetry of the toolpath parametrization

In this appendix, we elaborate about the square masonry block examples presented in Section 5.1. Therein, the adopted toolpath parametrization is symmetric with respect to the two principal symmetry axes of the block, except near the start and end points, where the toolpath is modified to ensure continuity. For square geometries with $N_{\mathrm{rx}} = N_{\mathrm{ry}}$, the overall design space may also be considered diagonally symmetric. However, the toolpath passage in the connection regions between adjacent rhombic cells is not necessarily symmetric with respect to the diagonal axis.

This is illustrated in Figure A1 for a square block with $N_{\mathrm{rx}} = N_{\mathrm{ry}} = 3$, $N_{\mathrm{seg}} = 3$, and $N_{\mathrm{outer}} = 2$, where the regions responsible for the loss of diagonal symmetry are highlighted by blue circles. The red dotted lines in the lower circle indicate the diagonally mirrored counterpart of the corresponding upper connection region. This geometric asymmetry results in a density field that is not perfectly symmetric with respect to the diagonal axis. Although these differences are very small and localized, they introduce a slight bias into the optimization problem.

To mitigate this effect, a simple symmetry-enforcing regularization strategy is adopted. Specifically, for the square block examples solved using Formulation #1, the sensitivities of pairs of diagonally symmetric design variables are replaced by their average,

$$\frac{\partial f}{\partial x_i} = \frac{\partial f}{\partial x_j} = \frac{1}{2}\left(\frac{\partial f}{\partial x_i} + \frac{\partial f}{\partial x_j}\right),$$

where x_i and x_j denote a pair of design variables related by diagonal symmetry. The same averaged sensitivity is then assigned to both variables, promoting symmetric design updates while preserving the overall sensitivity magnitude and avoiding the introduction of additional design variables or geometric constraints.

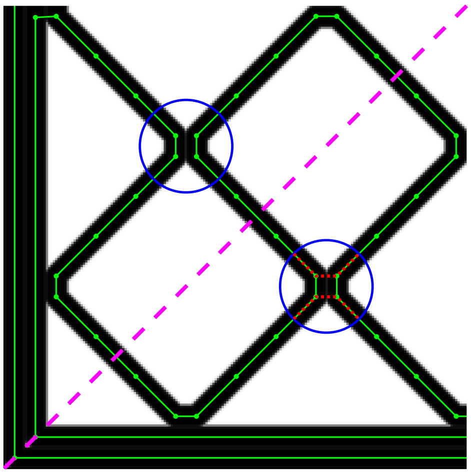

Fig. A1: Loss of diagonal symmetry in the toolpath parametrization and its effect on the resulting density field. Regions where the density field slightly differs from their diagonally mirrored counterparts are indicated by blue circles.

References

Anton, A., Reiter, L., Wangler, T., Frangez, V., Flatt, R.J., Dillenburger, B.: A 3D concrete printing prefabrication platform for bespoke columns. Automation in Construction **122**, 103467 (2021) https://doi.org/10.1016/j.autcon.2020.103467

Boissier, M., Allaire, G., Tournier, C.: Additive manufacturing scanning paths optimization using shape optimization tools. Structural and Multidisciplinary Optimization **61**(6), 2437–2466 (2020) https://doi.org/10.1007/s00158-020-02614-3

Bhooshan, S., Bhooshan, V., Dell'Endice, A., Chu, J., Singer, P., Megens, J., Van Mele, T., Block, P.: The Striatus bridge: Computational design and robotic fabrication of an unreinforced, 3D-concrete-printed, masonry arch bridge. Architecture, Structures and Construction, 1–23 (2022) https://doi.org/10.1007/s44150-022-00064-7

Breseghello, L., Naboni, R.: Toolpath-based design for 3D concrete printing of carbon-efficient architectural structures. Additive Manufacturing **56**, 102872 (2022) https://doi.org/10.1016/j.addma.2022.102872

Bruggi, M., Taliercio, A.: Design of masonry blocks with enhanced thermomechanical performances by topology optimization. Construction and Building Materials **48**, 424–433 (2013)

Bai, M., Xiao, J., Wu, Y., Ding, T.: Experimental and numerical study on the flexural behavior of 3D-printed composite beams with u-shaped ecc formwork. Engineering Structures **312**, 118225 (2024) https://doi.org/10.1016/j.engstruct.2024.118225

Carstensen, J.V.: Topology optimization with nozzle size restrictions for material extrusion-type additive manufacturing. Structural and Multidisciplinary Optimization **62**(5), 2481–2497 (2020) https://doi.org/10.1007/s00158-020-02620-5

Chen, X., Fang, G., Liao, W.-H., Wang, C.C.: Field-based toolpath generation for 3D printing continuous fibre reinforced thermoplastic composites. Additive Manufacturing **49**, 102470 (2022) https://doi.org/10.1016/j.addma.2021.102470

Coward, A., Sørensen, J.H.: 3D printed concrete beams as optimised load carrying structural elements–The Minimass beam. In: Structures, vol. 58, p. 105624 (2023). https://doi.org/10.1016/j.istruc.2023.105624

Chen, Y., Zhang, W., Zhang, Y., Zhang, Y., Liu, C., Wang, D., Liu, Z., Liu, G., Pang, B., Yang, L.: 3D Printed concrete with coarse aggregates: Built–in–Stirrup permanent concrete formwork for reinforced columns. Journal of Building Engineering **70**, 106362 (2023) https://doi.org/10.1016/j.jobe.2023.106362

Fang, G., Zhang, T., Huang, Y., Zhang, Z., Masania, K., Wang, C.C.: Exceptional mechanical performance by spatial printing with continuous fiber: Curved slicing, toolpath generation and physical verification. Additive Manufacturing **82**, 104048 (2024) https://doi.org/10.1016/j.addma.2024.104048

Greifenstein, J., Letournel, E., Stingl, M., Wein, F.: Efficient spline design via feature-mapping for continuous fiber-reinforced structures. Structural & Multidisciplinary Optimization **66**(5), 1 (2023) https://doi.org/10.1007/s00158-023-03534-8

Guo, Y., Liu, J., Xu, S., Yaji, K., Yamada, T.: Topology optimization of additively manufactured continuous fiber-reinforced composites using B-spline components. Computer Methods in Applied Mechanics and Engineering **461**, 119224 (2026) https://doi.org/10.1016/j.cma.2026.119224

Gebhard, L., Mata-Falcón, J., Anton, A., Dillenburger, B., Kaufmann, W.: Structural behaviour of 3D printed concrete beams with various reinforcement strategies. Engineering Structures **240**, 112380 (2021) https://doi.org/10.1016/j.engstruct.2021.112380

Guest, J.K.: Imposing maximum length scale in topology optimization. Structural and Multidisciplinary Optimization **37**(5), 463–473 (2009) https://doi.org/10.1007/s00158-008-0250-7

Hasani, A., Dorafshan, S.: Transforming construction? Evaluation of the state of structural 3D concrete printing in research and practice. Construction and Building Materials **438**, 137027 (2024) https://doi.org/10.1016/j.conbuildmat.2024.137027

Kubalak, J.R., Root, N.J., Wicks, A.L., Williams, C.B.: Improving mechanical performance in material extrusion parts via optimized toolpath planning. Additive Manufacturing **80**, 103950 (2024) https://doi.org/10.1016/j.addma.2023.103950

Kim-Tackowiak, H., Carstensen, J.V.: Topology optimization of 3D-printed material architectures: Testing toolpath consideration in design. Materials & Design, 114700 (2025) https://doi.org/10.1016/j.matdes.2025.114700

Kim-Tackowiak, H., Schemmer, Z.H., Jewett, J.L., Wongsittikan, P., Carstensen, J.V.: Effect of fabrication restrictions on topology optimized 3D printed concrete structures. Additive Manufacturing, 105283 (2026) https://doi.org/10.1016/j.addma.2026.105283

Kubalak, J.R., Wicks, A.L., Williams, C.B.: Simultaneous topology and toolpath optimization for layer-free multi-axis additive manufacturing of 3D composite structures. Additive Manufacturing **104**, 104774 (2025) https://doi.org/10.1016/j.addma.2025.104774

Li, Y., Wu, H., Xie, X., Zhang, L., Yuan, P.F., Xie, Y.M.: FloatArch: A cable-supported, unreinforced, and re-assemblable 3D-printed concrete structure designed using multi-material topology optimization. Additive Manufacturing **81**, 104012 (2024) https://doi.org/10.1016/j.addma.2024.104012

Maroszek, M., Hager, I., Mróz, K., Sitarz, M., Hebda, M.: Anisotropy of mechanical properties of 3d-printed materials—influence of application time of subsequent layers. Materials **18**(16), 3845 (2025) https://doi.org/10.3390/ma18163845

Moelich, G.M., Kruger, J., Combrinck, R.: Modelling the interlayer bond strength of 3d printed concrete with surface moisture. Cement and Concrete Research **150**, 106559 (2021) https://doi.org/10.1016/j.cemconres.2021.106559

Maitenaz, S., Mesnil, R., Feraille, A., Caron, J.-F.: Materialising structural optimisation of reinforced concrete beams through digital fabrication. In: Structures, vol. 59, p. 105644 (2024). https://doi.org/10.1016/j.istruc.2023.105644

Raza, S., Manshadi, B., Sakha, M., Widmann, R., Wang, X., Fan, H., Shahverdi, M.: Load transfer behavior of 3D printed concrete formwork for ribbed slabs under eccentric axial loads. Engineering Structures **322**, 119148 (2025) https://doi.org/10.1016/j.engstruct.2024.119148

Ren, H., Wang, D., Liu, G., Rosen, D.W., Xiong, Y.: Concurrent optimization of structural topology and toolpath for additive manufacturing of continuous fiber-reinforced polymer composites. Computer Methods in Applied Mechanics and Engineering **430**, 117227 (2024) https://doi.org/10.1016/j.cma.2024.117227

Shakur, E., Amir, O.: An integrated computational framework for structural optimization of prestressed concrete structures with 3D-printed formwork. Engineering Archive. Preprint (2026). https://engrxiv.org/preprint/view/6284

Salet, T.A.M., Ahmed, Z.Y., Bos, F.P., Laagland, H.L.M.: Design of a 3D printed concrete bridge by testing. Virtual and Physical Prototyping **13**(3), 222–236 (2018) https://doi.org/10.1080/17452759.2018.1476064

Stromberg, L.L., Beghini, A., Baker, W.F., Paulino, G.H.: Topology optimization for braced frames: Combining continuum and beam/column elements. Engineering Structures **37**, 106–124 (2012) https://doi.org/10.1016/j.engstruct.2011.12.034

Sousa, L.C., Castro, C.F., António, C.C., Sousa, H.: Topology optimisation of masonry units from the thermal point of view using a genetic algorithm. Construction and Building Materials **25**(5), 2254–2262 (2011) https://doi.org/10.1016/j.conbuildmat.2010.11.010

Sales, E., Kwok, T.-H., Chen, Y.: Function-aware slicing using principal stress line for toolpath planning in additive manufacturing. Journal of Manufacturing Processes **64**, 1420–1433 (2021) https://doi.org/10.1016/j.jmapro.2021.02.050

Sakha, M., Raza, S., Wang, X., Fan, H., Pichler, N., Shahverdi, M.: Design optimization and assessment of stay-in-place 3D printed concrete formwork for slabs. Automation in Construction **181**, 106572 (2026) https://doi.org/10.1016/j.autcon.2025.106572

Stolpe, M., Svanberg, K.: An alternative interpolation scheme for minimum compliance topology optimization. Structural and Multidisciplinary Optimization **22**(2), 116–124 (2001) https://doi.org/10.1007/s001580100129

Svanberg, K.: The method of moving asymptotes - a new method for structural optimization. International Journal for Numerical Methods in Engineering **24**, 359–373 (1987) https://doi.org/10.1002/nme.1620240207

Sun, H.-Q., Zeng, J.-J., Xie, S.-S., Xia, J.-R., Yu, S., Zhuge, Y.: Mechanical and microstructural characterization of interlayer bonding in multi-material 3D-printed concrete. Cement and Concrete

Composites **165**, 106308 (2026) https://doi.org/10.1016/j.cemconcomp.2025.106308

Vantyghem, G., De Corte, W., Boel, V., Steeman, M.: Structural and thermal performances of topological optimized masonry blocks. In: Asian Congress of Structural and Multidisciplinary Optimization 2016, Nagasaki, Japan (2016)

Wu, J., Aage, N., Westermann, R., Sigmund, O.: Infill optimization for additive manufacturing: approaching bone-like porous structures. IEEE transactions on visualization and computer graphics **24**(2), 1127–1140 (2018) https://doi.org/10.1109/TVCG.2017.2655523

Wein, F., Mirbach, J., Angre, A., Greifenstein, J., Hübner, D.: Multi-layer continuous carbon fiber pattern optimization and a spline based path planning interpretation. Journal of Manufacturing Processes **135**, 375–387 (2025) https://doi.org/10.1016/j.jmapro.2025.01.038

Wang, L., Tian, Z., Ma, G., Zhang, M.: Interlayer bonding improvement of 3d printed concrete with polymer modified mortar: Experiments and molecular dynamics studies. Cement and Concrete Composites **110**, 103571 (2020) https://doi.org/10.1016/j.cemconcomp.2020.103571

Zhu, B., Nematollahi, B., Pan, J., Zhang, Y., Zhou, Z., Zhang, Y.: 3D concrete printing of permanent formwork for concrete column construction. Cement and Concrete Composites **121**, 104039 (2021) https://doi.org/10.1016/j.cemconcomp.2021.104039